ACS APPLIED ENERGY MATERIALS

www.acsaem.org

Article

Understanding the Cell Performance Along the Channel for Industrial PEM Water Electrolysis Operation

Niklas Hensle,* Jerónimo Horstmann de la Viña, Nico Winterholler, Justin Hoffmann, Stephan Armbruster, Adrian Lindner, André Weber, and Tom Smolinka

Cite This: *ACS Appl. Energy Mater.* 2025, 8, 7107−7124

Read Online

ACCESS | Metrics & More | Article Recommendations | Supporting Information

ABSTRACT: Proton exchange membrane (PEM) water electrolysis cells can be operated very flexibly and at high current densities. Increasing the current density above today's industrial standard, in combination with low loadings of the catalyst layer, is necessary to become more economical and resource-saving. The water consumption and gas evolution rate are proportional to the current density, leading to a significant difference in the volumetric water-to-gas ratio over the active cell area when operating at high current densities and low water flow rates. This study analyzes industrial-relevant PEM water electrolysis operation at high current densities of up to 7 A·cm^{-2}, measured in a segmented along the channel test cell with a 30 cm channel length. We present locally resolved measurements of current density, temperature, and impedance spectra and discuss variations of operating parameters and porous transport layer microstructure for low-loading catalyst-coated membranes. To achieve a deeper understanding of the observed phenomena, we compare conventional voltage breakdown analysis, done by subtracting ohmic overpotentials through high-frequency resistance measurements, and kinetic overpotential using Tafel analysis with distribution of relaxation times (DRT) and equivalent circuit modeling. At industrially relevant operation with water stoichiometries greater than 50, no relevant mass transport losses or membrane drying effects are observed along the channel. In cases of low stoichiometries, combined with the high heat dissipation of the reaction at high current densities, a significant temperature increase of more than 8 K and a high-frequency resistance reduction along the channel are observed. Investigations using low-loading catalyst-coated membranes and different porous transport layers reveal a high sensitivity of local clamping pressure on the polarization processes but less impact on the high-frequency resistance.

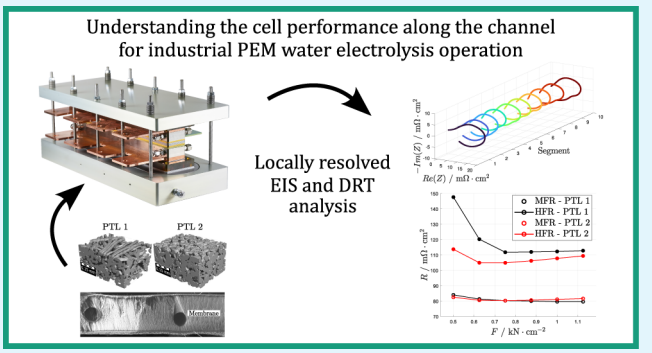

KEYWORDS: *PEM water electrolysis, segmented along the channel test cell, industrial-relevant operation, electrochemical impedance spectroscopy (EIS), distribution of relaxation time (DRT), equivalent circuit modeling (ECM), low catalyst loading, porous transport layers*

INTRODUCTION

Due to its possibility of being operated at high current densities and quickly be switched between different load levels, PEM water electrolysis has high potential to be coupled with renewable electricity from volatile wind and solar energy sources.[1−5] With the development of advanced components, like catalyst-coated membranes (CCMs) with a membrane thickness of less than 100 μm, operation at high current densities >5 A·cm^{-2} will be feasible in the future.[6−10] Even with low catalyst loading (<0.5 mg_{PGM}·cm^{-2}, PGM: platinum group metals), high cell efficiencies are realistic and intended by *Clean Hydrogen Partnership*, European Union and the *U.S. Department of Energy*, USA for future PEM water electrolysis operation.[11,12]

In principle, PEM water electrolyzers can be operated at way higher current densities (> 10 A·cm^{-2}), as shown in ref 7. In this work, we present polarization curve measurements using a laboratory-scaled cell up to 25 A·cm^{-2} under high water flow rates, without any indication of mass transport limitations, see Figure 1. Whether this phenomenon can also be seen on the industrial scale along the water supply channels is one of the key investigations in this work. However, when operating at high current densities, temperature issues must be considered due to the high heat dissipation rate induced by voltage loss (Joule heating). This consideration is important for performance as well as for degradation-based analyses, which require advanced thermal management within the cell.

Received: February 19, 2025
Revised: April 29, 2025
Accepted: May 2, 2025
Published: May 16, 2025

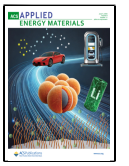

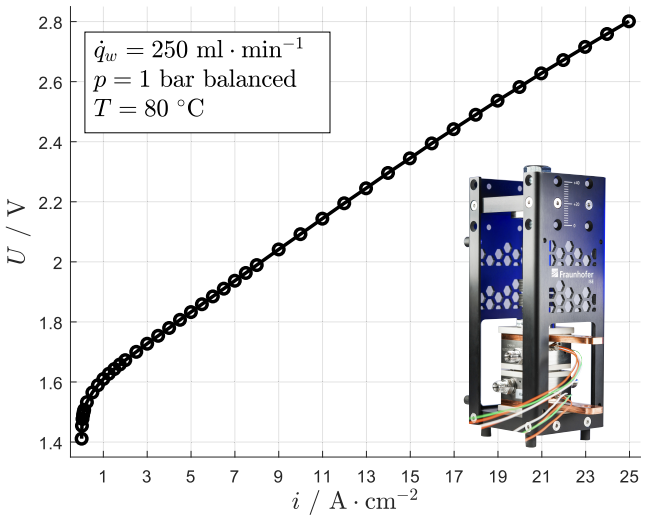

Figure 1. Polarization curve measured up to 25 A·cm^{-2} and 80 °C with our 4 cm² ISE reference cell (ambient pressure and a water flow rate of 62.5 ml·min^{-1}· cm^{-2} at the anode and cathode). The used CCM is in-house produced at Fraunhofer ISE with a 50 μm thick Nafion N212 membrane and a catalyst loading at the anode and cathode of (0.20 ± 0.07)mg$_{IR}$ cm^{-2} and (0.15 ± 0.03)mg$_{Pt}$ cm^{-2}, respectively.

With voltage−current breakdowns using the Tafel approach, Ohmic, kinetic, and "residual" overpotentials can be quantitatively determined. The residual overpotentials are often said to primarily consist of conventional fluidic (water and oxygen/hydrogen) mass transport-related overpotentials.[13−16] Others argue that besides fluidic transport within the catalyst and porous transport layer, the electronic and ionic transport in the catalyst layer needs to be considered in these overpotentials.[17−20] Padgett et al. demonstrated that the ionic and electronic resistivity is more relevant than conventional fluidic mass transport processes in PEM water electrolysis cells with low-loading catalyst layers.[18] This is in good agreement with our recent findings that low-frequency capacitive (mass transport related) processes in impedance spectra contribute minimally to the overall cell polarization.[21,22]

Instead, a process of inductive type that is not widely discussed in PEM water electrolysis becomes more pronounced with increasing current densities. In PEM fuel cells, the "inductive loop" can be detected in the Nyquist presentation of an impedance spectrum and is intensively discussed, often related to adsorption and desorption effects of intermediate species on the catalyst layer at the oxygen reduction reaction or to slow water transport in the ionomer.[23−26] Our previous publications on inductive loops at low frequencies in PEM water electrolysis show that this effect is a reproducible electrochemical process and not a measurement artifact.[21] We assume that this process is most likely related to a membrane effect at the anode and occurs at similar time constants as anodic mass transport processes.[22] Since the physico-chemical process of the inductive loop in PEM water electrolysis has not yet been completely understood, further experimental and simulative investigations must be conducted.

In industrial-scaled PEM water electrolyzers with active cell areas larger than 1000 cm², nonuniform cell conditions over the active area can occur and significantly influence the cell performance.[27,28] An uneven electrical contact of the components can lead to an ohmic-driven current density distribution that influences the cell utilization and might increase the overall contact resistance.[29] This compression-induced local current density distribution can lead to temperature hotspots due to the increased reaction rate. Furthermore, different ratios of water and gas can appear in the cell area. While there is a lot of water and less gas present at the cell inlet, high current density coupled with a low water flow rate can lead to a high amount of oxygen in volume fraction at the anode outlet.

To analyze the influence of different water and gas ratios, locally resolved measurements provide a deeper understanding. The so-called "along the channel" approach is the simplest method of spatially resolved measurement and enables a targeted investigation of effects along the water supply channels from the inlet to the outlet of the cell. Therefore, cells are designed with a small width but a long channel length. To improve the selectivity of the measurement, the cells are usually segmented to minimize transverse currents. In PEM water electrolysis, only a few works on locally resolved water are reported. Immerz et al. present a 50 cm² single-channel PEM water electrolysis cell with highly resolved current density, temperature, and impedance measurements along the channel.[27,29] Parra-Restrepo et al. show a 30 × 1 cm² multichannel segment cell with the possibility to conduct current density distribution measurements, analyzing the influence of different structural PTL parameters.[30] Dedigama et al. showed an 8.5 × 0.6 cm² segmented cell with current density monitoring and additional two-phase flow visualization along the channel.[31] Furthermore, locally resolved measurements on different test cell designs (circular, squared) are reported in refs[32−34]. The mentioned publications all have in common that they report relatively low mean current densities of <2 A·cm^{-2} when analyzing locally resolved measurements.

In this study, a recently designed and built up along the channel (AtC) test cell at *Fraunhofer ISE* is employed, see ref 28. With this test cell, highly resolved measurements of the current density and temperature distribution are feasible. However, to achieve a deeper understanding of polarization processes, the focus of the cell is to conduct locally resolved and segmented electrochemical impedance spectroscopy (EIS) with subsequent distribution of relaxation time (DRT) and equivalent circuit modeling (ECM). Complementarily, we present the voltage breakdown of polarization curve measurements.

With parameter variations at industrially relevant operation points, we analyze the channel and contact inhomogeneity effects. Sintered fiber and particle anode porous transport layers (PTLs) are employed to analyze the influence of different structural PTL parameters. For the in situ measurements, a commercial CCM with state-of-the-art catalyst layer loading and a CCM produced at Fraunhofer ISE with low catalyst loading are used. The latter CCM is in accordance with the US and EU development goals for PEM water electrolysis for the year 2030, see above.

EXPERIMENTAL SECTION

This section provides information about the test cell, the test bench, the implemented PTL and CCM materials, and the ex situ analysis methods used within this study. Furthermore, it shows our approach on the impedance analysis using DRT with subsequent equivalent circuit modeling and the polarization curve breakdown.

https://doi.org/10.1021/acsaem.5c00505
ACS Appl. Energy Mater. 2025, 8, 7107−7124

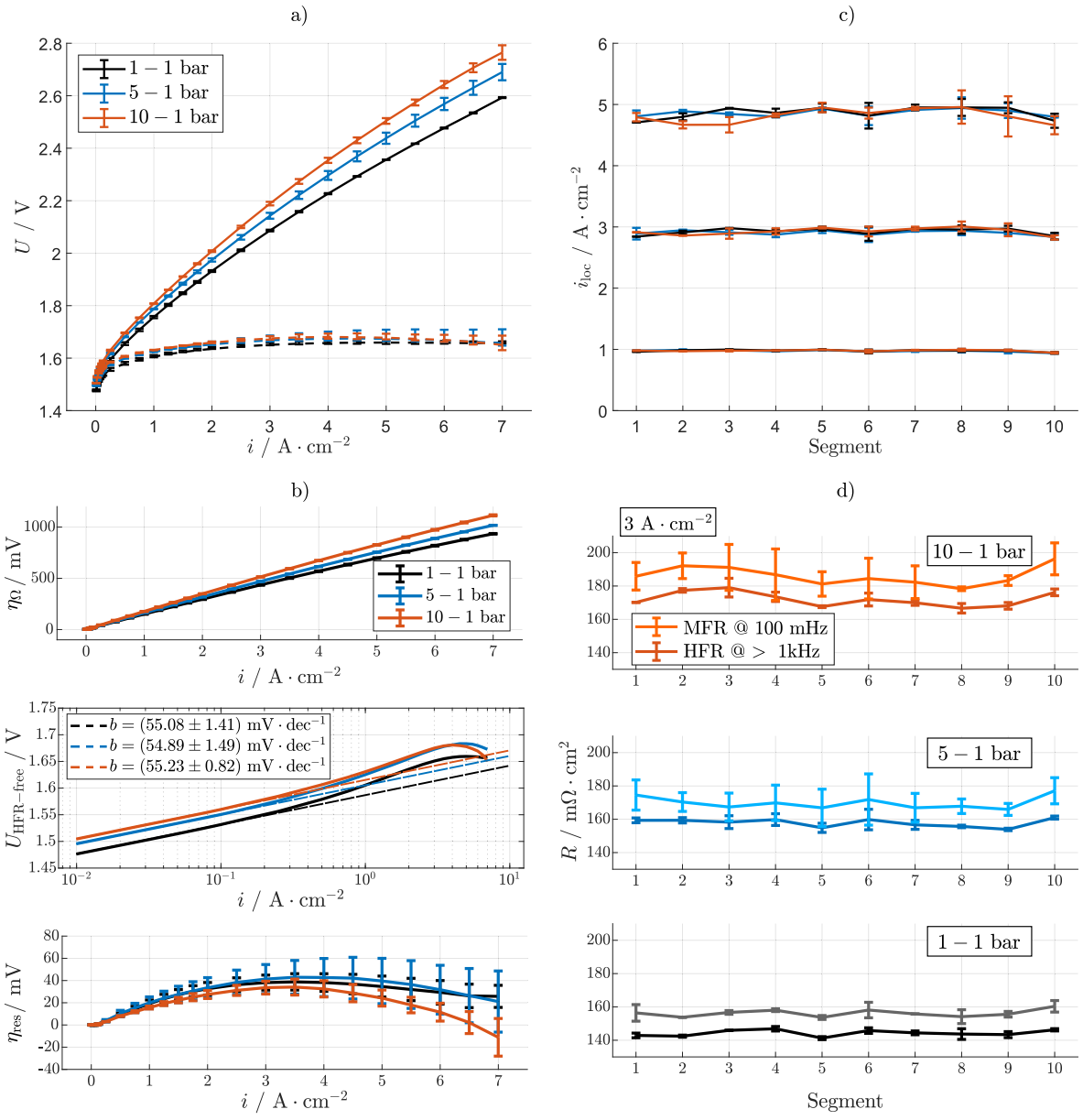

Figure 2. Variation of the cathode pressure between 1, 5, and 10 bar with always constant anode pressure of 1 bar (60 °C and anode flow rate of 10 ml·min^{-1}·cm^{-2}); (a) polarization curve and HFR-free polarization curve of the entire cell, (b) voltage breakdown analysis of the entire cell, (c) current density distribution at 1, 3, and 5 A·cm^{-2} mean current density, and (d) HFR and MFR distribution along the cell segments at 3 A·cm^{-2} mean current density.

AtC Cell Design and Test Bench. The AtC test cell used in this work[28] is designed and built at Fraunhofer ISE and has been described in more detail in our previous work. The cell has an active area of 30 × 2 cm (length × width) and is divided into 10 segments along the channel. To properly minimize the in-plane conductivity in the cell and to achieve highly selective measurements, the flow field plate and the PTL are segmented at the anode. The CCM and cathodic components are not segmented. The cell employs the measurement of the current density and temperature distribution with 40 contacts along the channel in three rows using a printed circuit board (PCB) custom designed by *DiLiCo Engineering GmbH*, Germany. Therefore, 3 × 4 measurement points are connected to each segment, leading to a total of 120 contacts. The local direct current (DC) density is measured with a shunt resistor approach, which involves the voltage drop over the known resistance of the shunt resistor. The temperature is measured at the same positions in a second layer within the PCB using Pt100 sensors. Both measurements are done with a four-electrode setup.

The locally resolved EIS is carried out using one central of the measurement contact in each segment, which is representative for all contacts since the current density difference of all measurement points within one segment is marginal (<0.5 % standard deviation). The alternating current (AC) response of the current density is analogous to the DC response determined by measuring the AC voltage drop over the shunt resistor using the frequency response analyzer (FRA) Zahner Zennium X in combination with Zahner EL1000 by *Zahner-Elektrik GmbH & Co. KG*, Germany and a third-party power supply. The AC voltage response of the cell is assumed to be constant in each segment and is therefore measured only

https://doi.org/10.1021/acsaem.5c00505
ACS Appl. Energy Mater. 2025, 8, 7107−7124

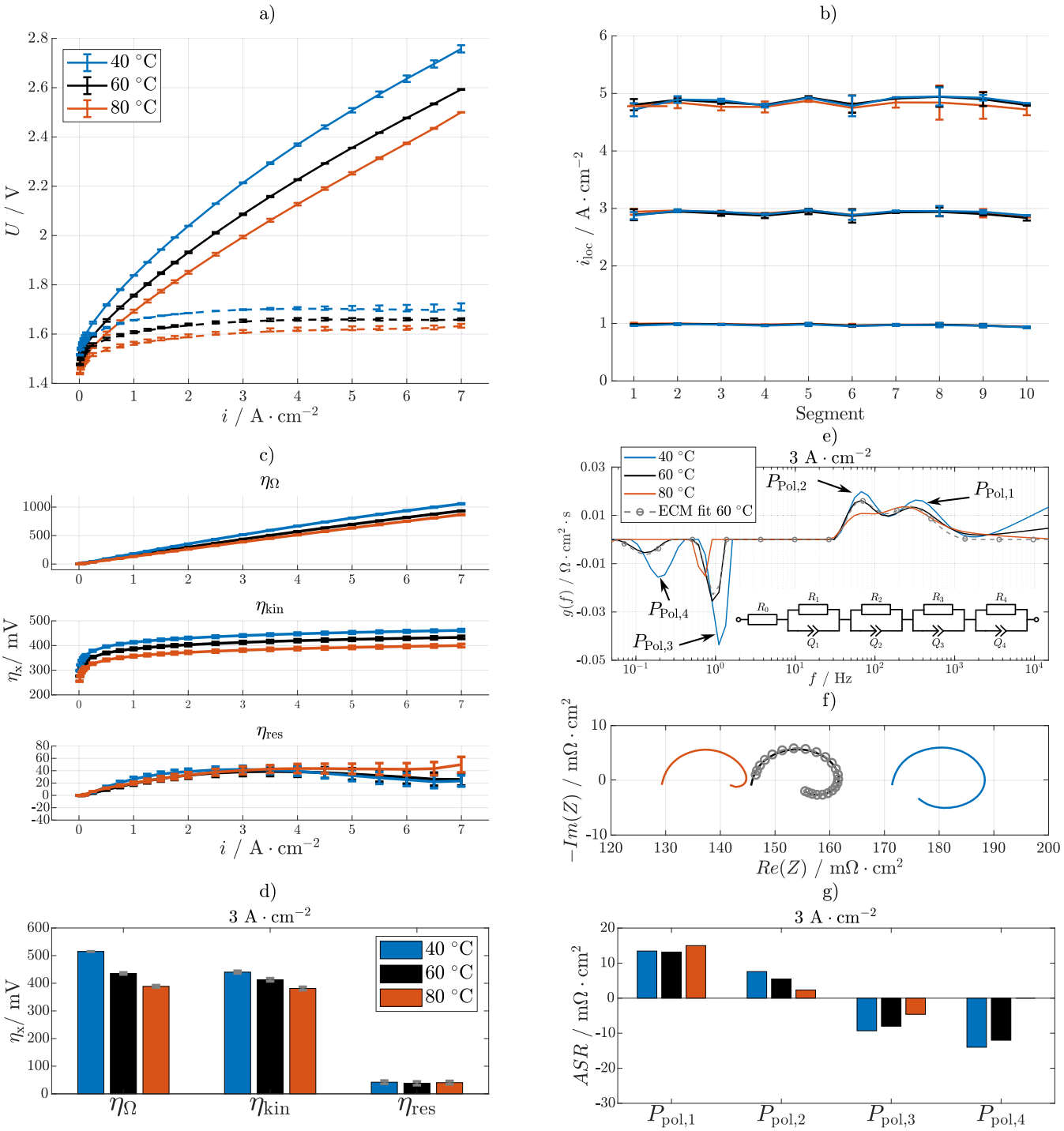

Figure 3. Temperature variation between 80 °C, 60 °C, and 40 °C at 1 bar_g balanced pressure and an anode flow rate of 10 ml·min^{-1}·cm^{-2}. (a) Polarization curve and HFR-free polarization curve of the entire cell, (b) current density distribution at 1, 3, and 5 A·cm^{-2} mean current density, (c) voltage breakdown analysis of the entire cell, (d) bar graph presentation of voltage breakdown at 3 A·cm^{-2}, (e) DRT analysis with ECM and ECM fit, (f) Nyquist presentation with ECM fit, and (g) analysis of ECM fit at 3 A·cm^{-2}.

at the center of the cell (segment 5). This assumption has previously been proofed, see ref 28. With the information on the mean cell AC voltage and the local AC current density in each segment, the impedance along the channel plus the mean cell impedance can be measured in parallel.

The test bench is an in-house built-up test bench at Fraunhofer ISE, which is designed for the operation with the AtC test cell up to 680 A (DC+AC) and 3 V, a pressure of 10 bar, a temperature of 80 °C, and a flow rate between 100 ml·min^{-1} and 1200 ml·min^{-1}. The water flow at the anode and cathode can be circulated within the test bench using inline ion exchangers to guarantee a low water conductivity at the anode and cathode. In this work, water is only fed to the anode.

For detailed information on the test cell and measurement technique, the test bench, and our discussion on the quality of the developed system, we refer to our previous work.[28] The measurements using the 4 cm^2 test cell shown in Figures 1 and 8 (for PTL 2, see below) are carried out on a comparable test

https://doi.org/10.1021/acsaem.5c00505
ACS Appl. Energy Mater. 2025, 8, 7107−7124

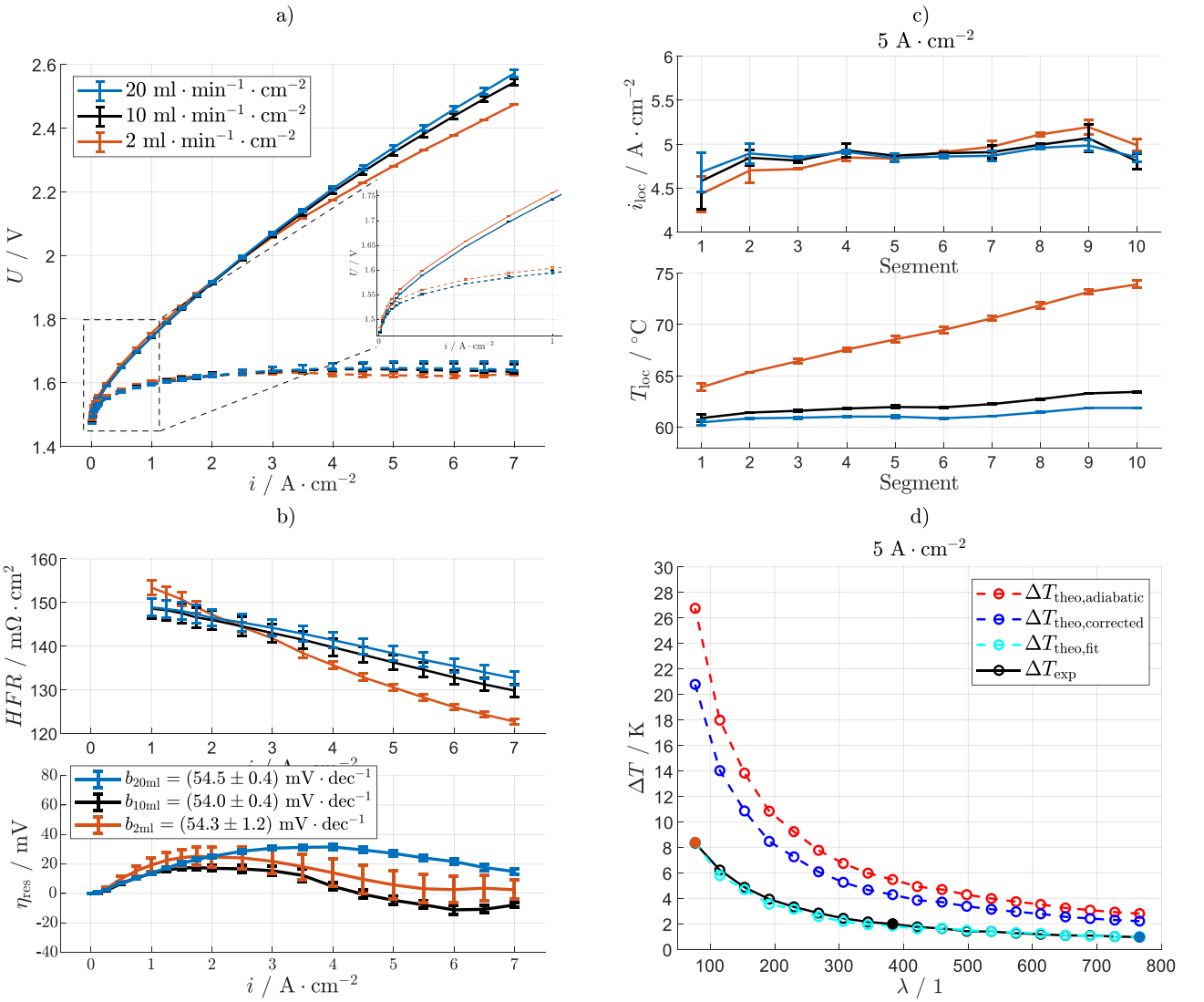

Figure 4. Water flow rate variation of 2, 10, and 20 ml·min^{-1}·cm^{-2} at 1 bar$_g$ balanced pressure and 60 °C. (a) polarization curve and HFR-free polarization curve of the entire cell and (b) mean cell HFR (top) and mean cell residual overpotentials (bottom) over current density, mean cell Tafel slope is given in the legend at the bottom. (c) Current density and temperature distribution at 5 A·cm^{-2} mean cell current density and (d) analysis of temperature difference between inlet and outlet at 5 A·cm^{-2} under variation of stoichiometry.

bench for single-cell testing. The different test benches used have not shown a measurable influence on the results.

Cell Materials and Ex Situ Characterization. *Porous Transport Layers.* The default anode PTL (here termed PTL 1) used in this study is a platinum-coated sintered titanium fiber PTL with 250 μm thickness. As the cathode PTL, a carbon-based gas-diffusion layer (here referred to as GDL) with a microporous layer (MPL) and 215 μm thickness is employed. For the analysis of different structural anodic PTL parameters, a sintered titanium particle PTL with 250 μm which was in-house platinum-coated is used, which we refer to as PTL 2. The structural parameters of the PTLs were investigated using mercury intrusion porosimetry (MIP) by *University of Gießen*, Germany[35] and micro-computer tomography (μ-CT) scans by KIT IAM-ET.

For the MIP, three samples per PTL are cut out at different positions across the PTL area (>20 × 20 cm²) to analyze the homogeneity of the materials and the pore size distribution. For μCT experiments, samples <1 cm × 1 cm were cut and fixed to a small metal pin. Samples were investigated with a Zeiss Xradia Versa 520 by Carl Zeiss AG, Germany using an accelerating voltage of 60 kV at 5 W power and 20× optical magnification resulted in a voxel size of 509 nm. For image processing, segmentation, and evaluation, we used the software toolbox GeoDict (Release 2024 from Math2Market GmbH, Germany https://www.geodict.com). Image data were processed by cropping a suitable region of interest, followed by nonlocal denoising. For segmentation, gray value thresholding based on Otsu[36] proved suitable.

We evaluated the three-dimensional PTL structure for grain and pore size distribution using the modules GrainFind and PoroDict, respectively. Pore space tortuosity was estimated by using DiffuDict. Figure 6a,b shows the results of the MIP and μ-CT analysis; the parameters that could be extracted from these measurements are summarized in Table 1.

Catalyst-Coated Membranes. As the default CCM, a commercially available E400 Gen.3 CCM by *Greenerity GmbH, Germany,* is employed. The catalyst layers are IrOx and Pt/C-based for the anode and cathode. The used membrane is a 125 μm Nafion-based (N115) membrane. More detailed informa-

https://doi.org/10.1021/acsaem.5c00505
ACS Appl. Energy Mater. 2025, 8, 7107−7124

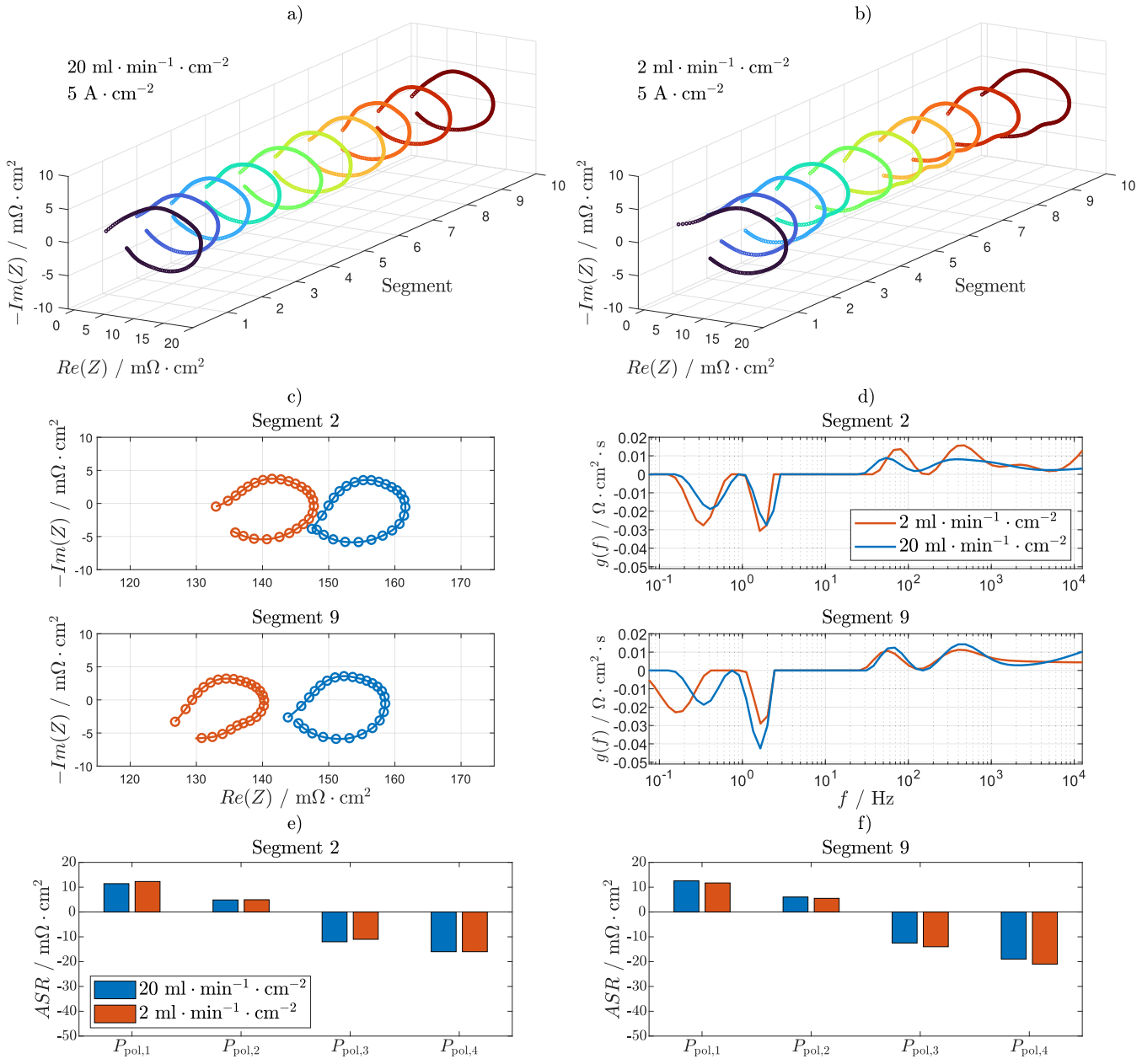

Figure 5. Water flow rate variation of 2 and 20 ml·min^{-1}·cm^{-2} at 5 A·cm^{-2}, 1 bar balanced pressure and 60 °C. HFR-free Nyquist presentation along the cell segments of (a) 20 and (b) 2 ml·min^{-1}·cm^{-2}. Impedance spectra of segment 2 and segment 9 in (c) as Nyquist plot including the HFR and (d) using DRT analysis. Results of ECM fit of segment 2 in (e) and segment 9 in (f).

tion on the catalyst loading and structure is not available for this commercial CCM, but in general, it shows high reproducibility and excellent lifetime and can be taken as an industrial benchmark for state-of-the-art membrane-electrode assembly (MEA) in PEM water electrolysis.

To investigate the impact of low loadings in combination with the variation of structural PTL parameters, an in-house produced CCM based on membrane FS-990-PK (90 μm thickness, reinforced) by *Fumatech BWT GmbH*, Germany is employed. Membrane samples were placed on a vacuum table, onto which anodic and cathodic catalyst inks were coated by using a 50 mm wide slot-die directly onto the membrane surface. The anodic ink was formulated with unsupported Iridium(IV)-oxide particles (Premion, 99.99%, 84.5% Iridium) by *ThermoFisher Scientific*, Germany dispersed in NPA-H20 solution combined with Fumion FSLA-1010 ionomer from *Fumatech BWT GmbH* at an ionomer-to-solid (I/S) ratio of 16.66 wt %. The total solid content of the ink was 24 wt %. The cathodic ink was prepared using platinum on carbon black particles (Elyst Pt50 0380, 50% Pt) by *Umicore AG & Co. KG*, Germany. This mixture was also dispersed in an NPA-Water solution combined with Fumion FSLA-1010 ionomer at an ionomer-to-carbon (*I*/*C*) ratio of 0.7, yielding a total solid content of 18 wt %. The catalyst layers were dried in a convection drier at 60 °C for 30 min and additionally hot pressed in a roll-to-roll laminator at 6 bar, 0.07 m/min, and 180 °C. The produced CCMs were in-house investigated using X-ray fluorescence spectroscopy (XRF) to analyze the homogeneity of the catalyst loading over the cell area for the anode and cathode. Using a scanning electron microscope (SEM), the CCM cross sections were analyzed for catalyst layer thickness homogeneity, as seen in Figure 6c, d.

https://doi.org/10.1021/acsaem.5c00505
ACS Appl. Energy Mater. 2025, 8, 7107−7124

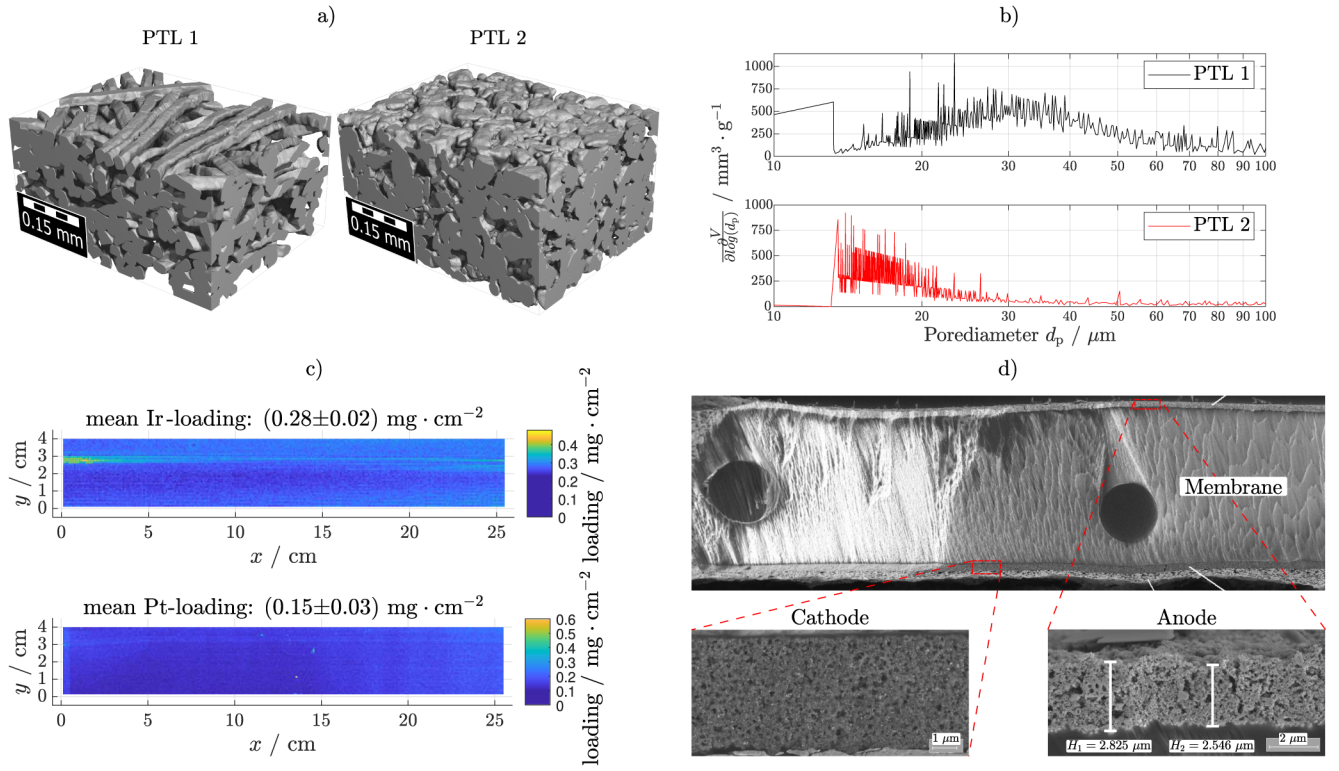

Figure 6. Microstructure analysis of commercial PTLs and low-loading CCM produced at the Fraunhofer ISE. (a) μCT-scans, (b) pore size distribution by MIP. (c) XRF analysis of the loading and its distribution of the anode (top) and cathode (bottom) catalyst layer, and (d) cross-sectional SEM scan of the CCM, the cathode and anode catalyst layer of the low-loading ISE CCM.

Electrochemical Measurements. The focus of this publication is electrochemical characterization using the AtC test cell described above. Therefore, we conduct polarization curve measurements between 0.01 and 7 A·cm^{-2}. The high-frequency series resistance (HFR) is measured at every current density point. Additionally, at specific operation points (0.1, 0.5, 1, 3, 5, and 7 A·cm^{-2}), EIS is conducted for the entire cell and all 10 segments in parallel. At each operation point, the current density and the temperature distribution are measured using the PCB. Furthermore, all data of the test bench, like water temperature, pressure, and flow rate, are measured. For a detailed description of the measurement methods employed, we refer to our previous work.[28]

Before each characterization, a CCM-specific break-in procedure is carried out. For the commercial CCM, water is flushed at 80 °C for 1 h, followed by current density steps at 0.2 and 1 A·cm^{-2} each for 30 min. Afterwards, constant voltage at 1.7 V is held for 12 h. For the ISE CCMs, a protocol is applied consisting of a 1 h water flushing at 80 °C, followed by five polarization curves in the same current density range as the later characterization and two constant voltage phases at 1.9 V for 5 h and 2.1 V for 10 h. Both break-in protocols have been proven to guarantee sufficiently stable cells for performance-based analyses.

The default operation point during characterization is 60 °C, 1 bar$_g$ balanced pressure, and a water flow rate at the anode of 10 ml·min^{-1}·cm^{-2} without applying water flow to the cathode. The temperature is varied between 40 and 80 °C, the pressure between 1 bar$_g$ balanced pressure, and 5−1 bar$_g$ and 10−1 bar$_g$ differential pressure with the higher pressure at the cathode. The flow rate is varied between 2 ml·min^{-1}·cm^{-2} (120 ml·min^{-1}), 10 ml·min^{-1}·cm^{-2} (600 ml·min^{-1}) and 20 ml·min^{-1}·cm^{-2} (1200 ml·min^{-1}). It is worth noting that today's industrial-operation points are usually driven with high stoichiometry >100 on which this study is focused on. The stoichiometry range in this study is between >54 and <380 000.

To make sure to analyze reproducible results and minimize the influence by internal contact of the segments, we conducted every measurement twice for the studies with commercial CCMs. This means that the cell was assembled with the same but pristine CCM and PTLs, and the identical measurement pretesting and protocol were run. Consequently, all figures in this work depict the mean value of both measurements, with error bars for the voltage response during a polarization curve. For the current density and temperature distribution, the mean value and error bars are also displayed. It is important to note that each cell assembly's current density profile is (slightly) influenced by the internal contact distribution given by the tolerances of the employed components. By carrying out pressure paper measurements and electrical current density profiles without CCM before each measurement, this influence is further minimized. Again, a detailed discussion can be found in our previous work.[28] All measurements with low-loading CCMs could not be repeated since not enough material from the same batch was available. Therefore, these results must be considered carefully, as reproducibility measurements are not conducted.

Electrochemical Analysis. For the polarization curve analysis, the breakdown of the ohmic, kinetic, and residual overpotentials is done. All impedance spectra are analyzed using the DRT approach, which was previously adapted to analyze low-frequency inductive features.[23] To ensure high impedance data quality, the Kramers−Kronig test is conducted

https://doi.org/10.1021/acsaem.5c00505
ACS Appl. Energy Mater. 2025, 8, 7107−7124

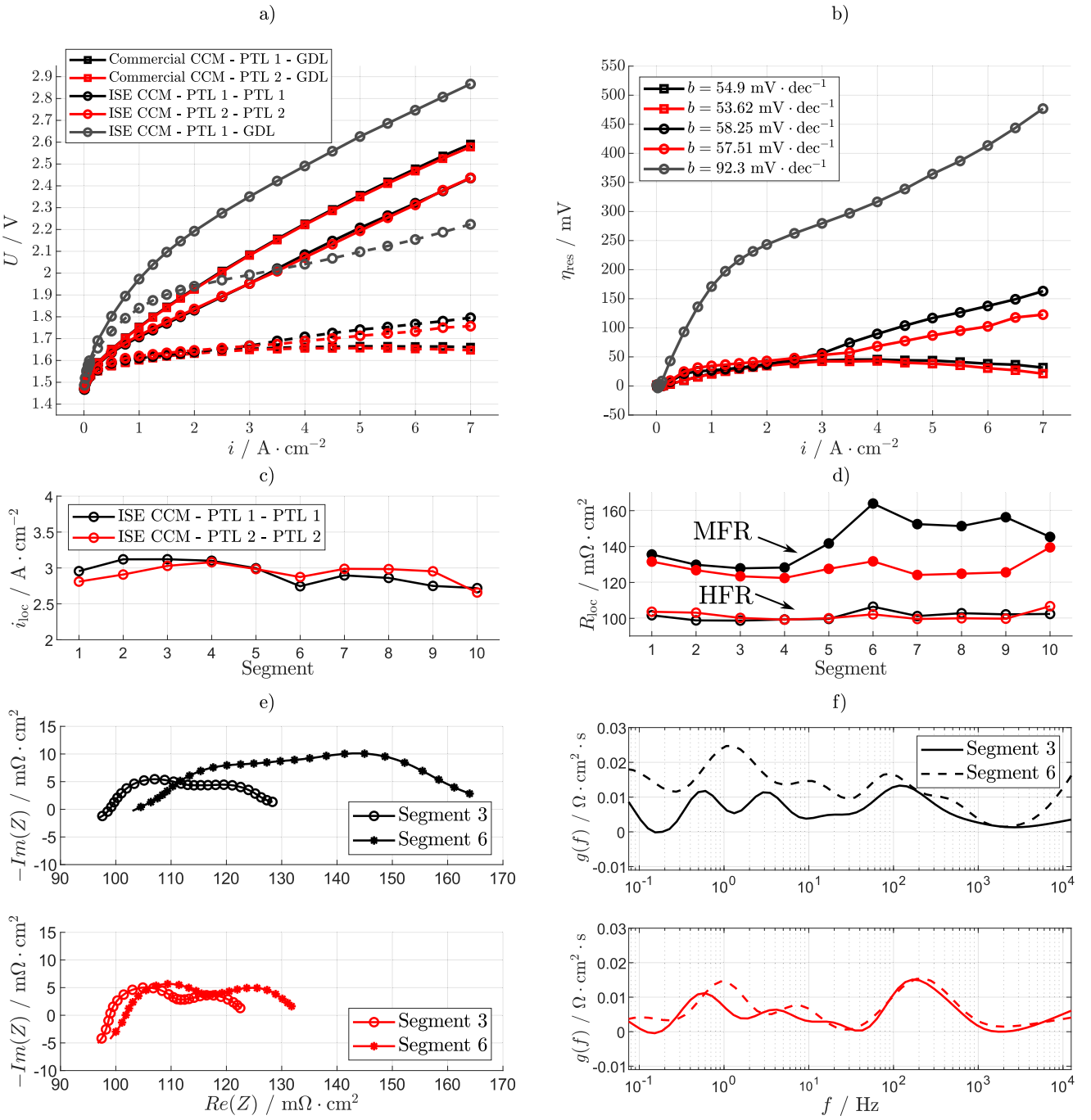

Figure 7. In situ analysis of PTL 1 and PTL 2 measured with the commercial CCM and the low-loading CCM produced at Fraunhofer ISE at 60 °C, ambient pressure and a water flow rate of 10 ml·min^{-1}·cm^{-2} at the anode. (a) Polarization curves and HFR-free polarization curves (dashed lines at the bottom) and (b) residual overpotentials. Analysis of the measurement with low-loading CCM and PTL 1 (black) and PTL 2 (red), (c) current density distribution, and (d) HFR and MFR distribution (bottom) at 3 A·cm^{-2}. Impedance analysis at 3 A·cm^{-2} of segments 3 and 6 in (e) Nyquist and (f) DRT presentation.

beforehand as described in ref 37. To quantify impedance data, we fit spectra and DRT using a fundamental ECM based solely on RQ elements, as presented in our previous publication.[22] The following sections provide a more detailed description of the evaluation methods used in this work.

Voltage Breakdown Analysis. The voltage breakdown of a polarization curve into the ohmic, kinetic, and residual overpotentials is a widely used method for PEM water electrolysis cells. Within this study, we provide the voltage breakdown for each polarization curve. Equation 1 shows the cell voltage and its breakdown into individual contributions.

$$U_{\text{cell}} = U_0(p, T) + \eta_{\Omega} + \eta_{\text{kin}} + \eta_{\text{res}} \quad (1)$$

$U_0(p,T)$ is the equilibrium cell voltage, which is temperature- and pressure dependent, and describable by the Nernst equation.[38] The temperature and pressure dependencies on the equilibrium cell voltage are approximated,[39−41] see eqs 2 and 3 with R being the general gas constant and F Faraday's constant. It is assumed that the influence on $U_0(p,T)$ does not

https://doi.org/10.1021/acsaem.5c00505
ACS Appl. Energy Mater. 2025, 8, 7107−7124

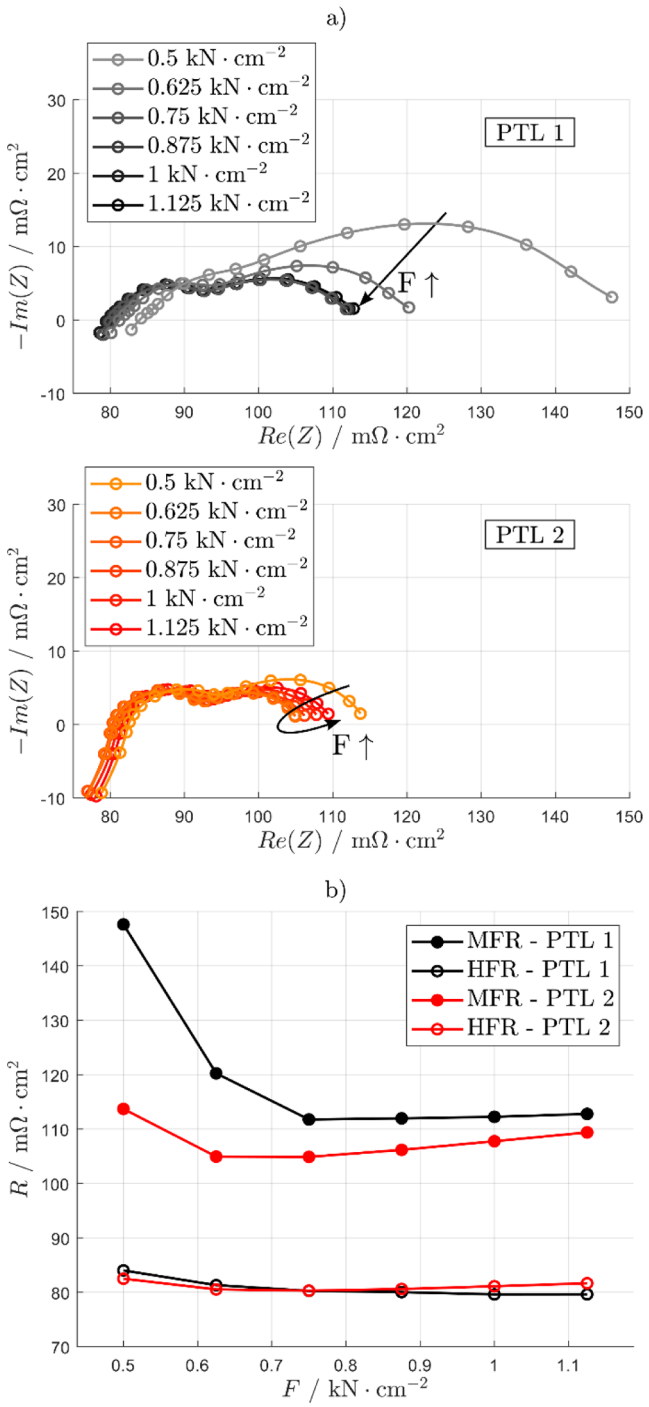

Figure 8. Clamping force variation of low-loading CCM with PTL 1 and PTL 2 in the 4 cm² Fraunhofer ISE reference cell. (a) Nyquist presentation at 3 A·cm⁻², 60 °C, ambient pressure and a water flow rate at the anode of 100 ml·min⁻¹ for PTL 1 at the top and PTL 2 at the bottom and (b) analysis of the HFR and MFR behavior at different clamping forces.

significantly change and therefore is assumed to be constant along the channel. η_Ω describes the ohmic, η_{kin} the kinetic, and η_{res} all residual overpotentials.

$$U_{i,0}(T) = 2F\Delta G(T) = 1.5184 - 1.5421\cdot10^{-3}\cdot T + 9.523\cdot10^{-5}\cdot T\cdot\log(T) + 9.84\cdot10^{-8}\cdot T^2 \quad (2)$$

Table 1. PTL Parameters Calculated from μCT Scans with the Software Tool GeoDict or Obtained from MIP Measurements

Sample	Median pore size/ μm (MIP)	Median pore size/ μm (μCT)	Porosity/ % (μCT)	Through-plane tortuosity/1 (μCT)	Surface Area/m^{-1} (μCT)
PTL 1	32.7	30.7	54.1	1.80	64 023
PTL 2	16.4	17.1	37.0	2.32	71 942

$$U_0(p, T) = U_0(T) + \frac{3R\cdot T}{4F}\cdot\log(p) \quad (3)$$

The ohmic contribution η_Ω includes all ionic, electrical bulk, and interfacial contact resistances and is quantified by measuring the HFR at each current density step. To minimize the error due to high-frequency artifacts induced by wiring, etc., we fit the impedance spectrum using an equivalent circuit model (ECM) in a specific frequency range and extract the HFR. For more detailed information, see the section Impedance Analysis and our previous publication.[28]

The impedance quality of the segments at current densities <1 A·cm⁻² is quite low due to the low AC voltage response, which is only a few mV. EIS is carried out with 10% amplitude of the DC operation point with the resistance of the shunt resistors being 33 mΩ. The voltage cards in use have a range of ±1 V; therefore, the signal-to-noise ratio is only valid for higher current densities, resulting in higher potential difference over the shunt resistor. The HFR at current densities <1 A·cm⁻² shows fitting errors of >3% and is therefore linearly extrapolated from the HFR at higher current densities for the cell segments and the entire cell. Since the HFR typically decreases linearly with increasing current density in this setup due to the positive temperature effect on the membrane resistance driven by increasing heat dissipation of the reaction. η_Ω can then be described by multiplying the HFR (R_{HFR}) with the current density j in segment i, see eq 4.

$$\eta_{i,\Omega} = R_{i,HFR}\cdot j \quad (4)$$

The kinetic contribution η_{kin} describes the kinetic overpotentials assuming that the electrode polarization at the cathode is negligible during the hydrogen evolution reaction (HER). Therefore, all kinetic overpotentials are assigned to the anode only. Equation 5 describes the determination of the kinetic overpotentials using the Tafel approach.[42]

$$\eta_\Omega = b\cdot\log\left(\frac{j}{1\text{A}\cdot\text{cm}^{-2}}\right) \quad (5)$$

With b describing the Tafel slope, which is determined by linearly fitting the HFR-free cell voltage during the polarization curve measurement plotted against $\log\left(\frac{j}{1\text{A}\cdot\text{cm}^{-2}}\right)$ in the low current density region between $0.01 < j < 0.1$. At these low current densities, the contribution of residual overpotentials can be considered negligible. By multiplying the Tafel slope by $\log\left(\frac{j}{1\text{A}\cdot\text{cm}^{-2}}\right)$ over the whole polarization curve, η_{kin} can be determined for each current density step.

The residual overpotentials η_{res} consist of diffusive and convective mass transport in the catalyst and the porous transport layers and ionic and electronic in-plane resistance of the catalyst layer, with the latter being the limitation for low-loading catalyst layers.[18,19] Furthermore, the influence of gas

https://doi.org/10.1021/acsaem.5c00505
ACS Appl. Energy Mater. 2025, 8, 7107−7124

crossover on the cell voltage might be included. η_{res} can be calculated according to eq 1.

Impedance Analysis. To determine the HFR of the entire cell and the individual segments, impedance measurements between 10 and 100 Hz are conducted. The HFR is subsequently determined by fitting the frequency region between 1 kHz and 100 Hz using an equivalent circuit model consisting of a resistor R_0 in series connection with an RQ element (resistor R_1 with a constant phase element (CPE_1) in parallel) for every segment and the entire cell. With this approach, we assume that only the anodic charge transfer is relevant in this frequency region. To extract the HFR, the model is extrapolated to frequencies >1 MHz, at which only the resistor R_0 is relevant. A detailed analysis of this method is discussed in our previous publication.[28]

At mean current densities of 0.1, 0.5, 1, 3, 5, and 7 A·cm^{-2}, impedance spectra of the entire cell and the 10 segments are additionally measured alongside the polarization curve measurements. The frequency range used is 10 kHz to 100 mHz. The whole impedance spectrum and the HFR measurements are done with a resolution of 10 points per decade and an integration time of 10 periods.

Kramers–Kronig Test. To properly analyze impedance spectra, high data quality is necessary. This need becomes even more pressing when analyzing the data using DRT since measurement artifact might be detected as processes and therefore lead to misinterpretations.[43] Conducting the Kramers–Kronig test is therefore a well-established procedure to analyze the impedance data for stability, linearity, and causality.[37] To ensure high data quality, we use a method of the Kramers–Kronig test presented in ref 44. This method allows us to analyze, beside the conventional capacitive polarization, also the low-frequency inductive polarization. All shown impedance spectra in this study fulfill the Kramers–Kronig test, with residuals being below ±1%.

Distribution of Relaxation Time (DRT). The DRT analysis of impedance spectra is well-established for several electrochemical applications, such as batteries and fuel cells.[45−48] For PEM water electrolysis, relatively few studies have published using the DRT approach.[22,49−51] When the polarization processes are not fully understood and equivalent circuit models cannot be confidently applied to certain processes, DRT analysis can deconvolute the different electrochemical processes in the cell, visualize their operating parameter dependencies, support the development of meaningful equivalent circuit models, and provide starting values for the subsequent complex nonlinear least-square fitting (CNLS fitting). This fact is relevant for low-frequency impedance analysis in PEM water electrolysis, since modeling of mass transport-related polarization is not fully understood, as evidenced by the different equivalent circuit elements used.[52] Furthermore, low-frequency inductive behavior is with one exception[53] and beside our previous work[21,22] not discussed in PEM water electrolysis.

In this work, the DRT was calculated via the Tikhonov regularization[54] using an algorithm suggested by Weese,[55] which was implemented in Matlab. The Tikhonov regularization parameter was identified to be most suitable for these measurements with $\lambda = 10^{-3}$, see Figure S1. Since the impedance at low frequencies and higher current density shows an inductive feature, a previously adapted version[23] of this DRT algorithm was applied. In this approach, RC elements with negative resistance and capacitance values are used[56] for the low-frequency range of the spectra.

Equivalent Circuit Modeling. For the analysis and quantification of impedance data, equivalent circuit modeling is a widely used approach. In PEM water electrolysis, some works has been reported on the use of ECMs to determine charge transfer and mass transport-related polarization resistances.[57−60] For charge transfer analysis, usually an RQ element for the cathode and another one for the anode are used, with the cathode often being neglected due to its small contribution to the overall charge transfer resistance.

As mentioned above, low-frequency analysis of impedance by ECM differs from that in the literature. For the low-frequency inductive feature, no specific element has been reported for PEM water electrolysis. The relaxation impedance reported by Goehr and Schiller can be used to model low-frequency inductive features, depending on the potential and changes in the structural properties of porous electrodes and double-layer formation.[61] But this model has been adapted only to describe the surface change at carbon monoxide poisoning of the cathode in PEM fuel cells.[62] Since the origin of the inductive loop in PEM water electrolysis is not understood yet, it significantly overlaps with low-frequency capacitive (mass transport-related) polarization (see our previous publication,[22] we here choose an equivalent circuit model that employs only RQ elements, see Figure 3e). Therefore, the number of relevant processes is detected using DRT, and subsequently, the impedance data are fitted to determine both capacitive and inductive processes, using as many RQ-elements as peaks detected in the DRT. With a proper fit of the ECM to impedance data and DRT, we can determine the area-specific resistance (ASR) of each process deconvoluted by the DRT analysis. For the inductive processes, we allow negative values for the RQ-elements, as presented in refs [22,23]. This allows us to properly determine charge transfer resistances and quantitatively analyze the low-frequency impedance.

RESULTS AND DISCUSSION

Measurements with our standard 4 cm² laboratory test cell[63] show no mass transport limitations. Even at high current densities of up to 25 A·cm^{-2}, a linear behavior without any exponential voltage increase due to diffusion or conversion limitations is observable when operating with high water stoichiometries, see Figure 1. This is even valid for the here used low-loading CCM produced at Fraunhofer ISE with an iridium loading of (0.20±0.07) mg·cm^{-2} for the anode, a platinum loading at the cathode of (0.15 ± 0.03) mg·cm^{-2} and a 50 μm thick Nafion (N212) membrane. As PTLs, 250 μm thick platinum-coated titanium fiber PTLs are used for both sides, which seem to enable sufficient water supply and gas removal.

At 3 A·cm^{-2}, a cell efficiency referred to the thermal neutral cell voltage (1.49 V at 80 °C) of more than 86% was measured, meeting the EU and US performance and material development targets for the year 2030.[11,12] The cell efficiency might be increased even further by using thinner membranes. However, aspects such as gas crossover and durability must be considered carefully at these operation points.

Due to the high water flow rate of 62.5 ml·min^{-1}·cm^{-2} applied, corresponding to a stoichiometry of >445 at 25 A·cm^{-2} (~37 % water in volume fraction at the anode under operation condition), an undersupply of water on a macroscale

https://doi.org/10.1021/acsaem.5c00505
ACS Appl. Energy Mater. 2025, 8, 7107−7124

does not play a significant role. In other words, with the amount of water applied to the cell, a maximum hydrogen production of 311 Nl·min^{-1} can be realized, which corresponds to 44 kA current applied to the cell. With the here produced 25 A·cm^{-2} (100 A absolute), a water utilization of only 0.22 % and an oxygen-to-liquid volume ratio of 1.39 and hydrogen-to-liquid volume ratio of 2.79 under normal conditions are present.

This indicates that today's porous materials can properly distribute the water as a reactant to the catalyst particles even though high evolution rates of gas are present. When operating with long water supply channels, accumulation of gas might lead to a critical water-to-gas ratio, which is investigated in the following.

Performance Analysis Along the Channel. *Differential Pressure Variation.* The results of differential pressure variation in the AtC test cell are summarized in Figure 2. The entire cell polarization curve and the HFR-free polarization curve (dashed lines at the bottom) are shown for 1 bar$_g$ balanced pressure, 5 to 1 bar$_g$ and 10 to 1 bar$_g$ differential pressure at 60 °C and 10 ml·min^{-1}·cm^{-2} in Figure 2a. The polarization curves show a decreasing performance with increasing differential pressure. The HFR-free polarization curves indicate that the differences are mostly related to different Ohmic resistances, as shown by the Ohmic overpotential in Figure 2b. This behavior is unexpected for the comparably low differential pressures based on our previous work,[28] where no influence of differential pressure on the Ohmic resistance was detected. Although the cell setup is comparable in both studies, in this work, we use a thinner anode PTL with only 250 μm instead of previously used 500 μm thick PTLs, but the same GDL and CCM. Therefore, we attribute this increased Ohmic resistance at higher differential pressure to a worse electrical contact at the anode. With higher gas pressure at the cathode, the thin PTL may be pressed more into the channel and bending over the 1 mm channel width, which leads to a decreased electrical contact between the PTL and the flow field lands. Furthermore, the increased gas pressure may cause detachment of the GDL at the cathode, resulting in additional increased contact resistance. A better balance of flow field and PTL design should minimize this effect, which is not the focus of this study.

The HFR-free polarization curve exhibits a higher voltage of ∼29 mV between 1 bar$_g$ and 10 bar$_g$ cathode pressure at low current densities, which can be referred to increasing Nernst potential with higher hydrogen pressure, see eq 3. With increasing current density, the three HFR-free curves converge, as kinetic and residual overpotential show smaller contribution at higher gas pressure, see Figure 2b. The kinetics do not differ significantly, as noted in the legend of the $U_{\text{HFR-free}}$ graph in Figure 2b. The decreasing residual overpotentials may be explained by better electronic and ionic conductivity between catalyst particles due to higher compression at the anode of the PTL and the catalyst layer. Additionally, the gas transport at the cathode should be increased since hydrogen needs less volume at higher pressure which may also contribute to this. Please note that for high current densities, negative values for the residual overpotentials occur. This is a nonelectrochemical artifact and is related to the increase in cell temperature with increasing current density and inaccuracies of the voltage breakdown calculation. This phenomenon is visualized by the Tafel slope and the intersection with $U_{\text{HFR-free}}$ at current densities above 6 A·cm^{-2}, see Figure 2b in the center.

Figure 2c shows the current density distribution along the cell segments at different mean current densities. The parallel measured temperature profile is provided in Figure S2. For low current densities, the profiles are in good consistency, and the maximum error due to different contact of the segments is below 80 mA·cm^{-2}. However, as the mean current density increases, contact issues become more relevant. At 5 A·cm^{-2} and 10 to 1 bar$_g$ pressure operation, the segments are better contacted in the center and less at the inlet and outlet of the AtC cell. This is attributed to slightly better compression in the cell center and an amplifying effect due to the increased gas pressure. As expected, no effect along the channel occurs with increased cathode gas pressure. The temperature profiles show neither a significant temperature gradient influenced by the differential pressure (Figure S2) nor a significant gradient along the channel segments. This is explained by the high water flow rate of 10 ml·min^{-1}·cm^{-2} (noncritical water-to-gas ratio >26 vol % at the cell outlet at 7 A·cm^{-2}), which was purposely chosen to realize homogeneous temperature profiles. This is also illustrated by the HFR and MFR (minimal frequency resistance, measured through EIS at 100 mHz) distribution, exemplarily shown for 3 A·cm^{-2} in Figure 2d. Both resistances are influenced by the contact issues discussed above and exhibit no converging or diverging effects along the channel, which can be interpreted as a constant polarization resistance. For a cathode pressure of 5 bar$_g$ and 10 bar$_g$, the HFR is reproducible, but the MFR shows larger error bars compared to the 1 bar$_g$ balanced pressure. We refer to this as a more unstable situation of the cell at higher gas pressure.

Temperature Variation. The temperature variation shows, as expected, decreasing performance with decreasing temperature, as summarized in Figure 3a. The temperature is varied between 80 and 40 °C at 1 bar$_g$ balanced pressure and a water flow rate of 10 ml·min^{-1}·cm^{-2}. The polarization curves and the HFR-free polarization curves show at high current densities a cooling effect at 80 °C and a heating effect at 40 °C, which can be seen in the decreasing and increasing slopes, respectively. The 60 °C graphs remain relatively linear. This effect can also be seen at the temperature differences along the channel. Although the temperature profiles, see Figure S3, do not appear to be significantly affected by different cell temperatures (the temperature difference along the channel even at 5 A·cm^{-2} does not exceed 3 K), it clearly shows that at 40 °C the cell is heated up, as the temperature gradient to the surrounding (20 °C) is lower compared with 60 and 80 °C operation. Figure 3b indicates that there is no detectable effect along the channel with varying temperature.

The voltage breakdown of the entire cell is shown in Figure 3c and indicates that, alongside the Ohmic overpotentials, the kinetic overpotentials also increase with decreasing temperature. This is attributed to decreasing membrane conductivity and the higher activation energy needed for the reaction, as less energy is available from thermal sources. The residual overpotentials are in good agreement with each other for current densities <4 A·cm^{-2} but show slightly increased overpotentials for higher current densities at 80 °C. Diffusion-related overpotentials usually increase with temperature, as the gas diffusion coefficient decreases. For this high-loading catalyst layer, we do not believe that the in-plane resistance of the catalyst layer plays a major role. To facilitate comparison between the voltage breakdown analysis and impedance analysis, Figure 3d highlights the voltage breakdown for 3 A·cm^{-2} in a bar graph format.

https://doi.org/10.1021/acsaem.5c00505
ACS Appl. Energy Mater. 2025, 8, 7107−7124

Figure 3e shows the impedance analysis using DRT at 3 A·cm^{-2} for the temperature variation. Additionally, the results of the ECM fit are exemplarily shown for the measurement at 60 °C. The schematic presentation of the used ECM is displayed at the bottom right. Four significant peaks are identified by DRT analysis for all three measurements at different temperatures. As explained above, each peak can be referred to a single polarization process ($P_{Pol,1}$ to $P_{Pol,4}$), and the resulting ECM fit at 60 °C is in good agreement with the measurement data for frequencies <1 kHz. Due to artifacts induced by wiring and the cell itself, higher frequencies cannot properly be fitted with the ECM used here since no inductive element is used. It should also be noted that this may influence the evaluation of the resistance of $P_{Pol,1}$. The corresponding Nyquist plots of the impedance measurement and the ECM fit for 60 °C are provided in Figure 3f.

Figure 3g shows the bar graph presentation of the ASR extracted from the DRT data for the temperature variation at 3 A·cm^{-2}. $P_{Pol,1}$ can be detected between a peak frequency of 250 to 350 Hz. The corresponding ASR shows slightly higher resistance at 80 °C but comparable values at 40 °C and 60 °C. $P_{Pol,2}$ is detected between 60 and 80 Hz, and the ASR hereby decreases with increasing temperature. It should be noted that the ASR corresponds to the area underneath the DRT peak and not to the peak height. The behavior of $P_{Pol,2}$ is a characteristic of charge transfer behavior, and the behavior of $P_{Pol,1}$ is rather atypical. Since we avoided low values for the regularization parameter λ to minimize misinterpretation, we believe that the separation of both processes is not accurately the same for the impedance measured at different temperatures, which can be observed in the different dilatation of the peaks. Therefore, we sum up process $P_{Pol,1}$ and $P_{Pol,2}$ and assume that the sum includes the share of anodic and cathodic charge transfer.

$P_{Pol,3}$ (between 0.7 and 1.2 Hz) exhibits a typical behavior for the low-frequency inductive feature with an increasing ASR with decreasing temperature. This is consistent with our previous works.[21,22] We believe that the inductive process is related to a membrane effect that may be led or at least is accelerated with local temperature, which is more relevant when operating at lower cell temperature. Between 0.1 and 0.25 Hz, a second inductive peak is recognizable. $P_{Pol,4}$ shows for the 40 °C measurement quite high negative values of the ASR. The 60 °C measurement also shows a second inductive feature; at 80 °C, no second inductive feature is detected. To our knowledge, there is no clear understanding of the physical significance of one or both inductive features; for further discussion on this, we refer to.[22] As no low-frequency capacitive process is detectable, mass transport-related processes do not seem to play a dominant role or are superimposed by inductive features. This is in good agreement with recent studies showing that mass transport- or diffusion-related polarization is typically not much relevant when operating at high water stoichiometries.[18]

Water Flow Rate Variation. Figures 4 and 5 show the results of the variation of the water flow rate at the anode. The polarization curve and the HFR-free polarization curve of the entire cell are given in Figure 4a; the HFR and residual overpotentials are shown in Figure 4b. For low current densities (<3 A·cm^{-2}), only small differences in the polarization curve are detected, with the low flow rate (orange graph) showing the highest overpotentials and the high water flow rate (blue graph) showing the lowest overpotentials, as seen in the zoomed-in section. At a higher current density of >3 A·cm^{-2}, the behavior changes, and the overpotentials decrease with decreasing flow rate. We refer this trend to a temperature effect, which is typical when comparing different water flow rates without the use of an external heat management but only an internal heat management of the cell. With the high heat dissipation at high current densities, low water flow rates lead to higher temperature at the electrochemically active parts of the CCM. For high water flow rates, the water temperature and thus the CCM temperature are increasing less. Therefore, the cell temperature and hence the performance of the cell are increased with less water applied, compare as well with the temperature profile in Figure 4c. This phenomenon indicates better performance with a lower water flow rate. As the performance improvement is related to a higher CCM temperature, this is accompanied by higher stress levels that may affect the durability of the cell.

Figure 4c shows the current density and temperature profiles along the channel for a mean current density of 5 A·cm^{-2}. The profiles for the mean current densities of 1 and 3 A·cm^{-2} are given in Figure S4. At low mean current densities, a stable current density distribution of the segments along the channel can be observed for all flow rates. The temperature profile is in accordance with the lower performance for low water flow rates at <3.0 A·cm^{-2} as a difference of approximately 3 K can be seen between 2 and 20 ml·min^{-1}·cm^{-2}. For flow rates of 10 and 20 ml·min^{-1}·cm^{-2}, still stable temperature profiles and current densities along the cell segments are measured at a mean current density of 5 A·cm^{-2}. For the lowest flow rate of 2 ml·min^{-1}·cm^{-2}, a temperature gradient of >8 K is measured, which strongly affects the current density distribution, leading to an increase in current density of ∼0.5 A·cm^{-2} between the inlet and outlet.

These temperature effects can also be seen when analyzing the mean cell HFR at different current densities; see Figure 4b. At low water flow rates, the HFR decreases drastically between 1 and 7 A·cm^{-2}, while the HFR at the higher flow rates does not decrease that much. Also, the intersection at 2.5 A·cm^{-2} agrees with the intersection of the polarization curves. The calculated Tafel slopes (depicted in the legend of Figure 4b at the bottom) do not reveal any differences in the measurements and show a similar kinetic behavior at low current densities (<0.1 A·cm^{-2}) for all flow rates. The residual overpotentials do not show a clear trend and do not reveal that there are any mass transport-related overpotentials occurring during this water flow rate variation.

Figure 4d shows the measured temperature difference between the inlet and outlet for a highly resolved stoichiometry variation at 5 A·cm^{-2} mean cell current density (black graph). The three flow rates used in Figure 4a−c are marked with the corresponding colors. The measured range corresponds to an outlet water-to-gas ratio of ∼9 vol % to ∼50 vol %. As assumed, a highly nonlinear dependency between the temperature difference and water flow rate is detected. Based on a general rule of thumb, a temperature difference of 3 K between the inlet and outlet is suggested not to be exceeded for proper and long-term stable cell operation. According to our data, this is achieved at a water amount of less than 26 vol % corresponding to a stoichiometry of ∼268 or >6 ml·min^{-1}·cm^{-2}.

Since the AtC test cell is neither thermally insulated nor equipped with external heating, the heat dissipation is not negligible. To estimate the heat dissipation, the theoretical

https://doi.org/10.1021/acsaem.5c00505
ACS Appl. Energy Mater. 2025, 8, 7107−7124

temperature difference between the inlet and outlet, under the assumption of an adiabatic system, is calculated (see red graph). By measuring the temperature difference between the inlet and outlet (segments 1 and 10) at negligible reaction heat (i = 0.01A cm^{-2} and U = 1.484 V), the heat loss through the PCB is estimated to be $\dot{Q}_{loss,PCB}$ = 49.41 W, which corrects the adiabatic graph (see blue graph). To analyze the additional heat loss to the surrounding, the corrected curve is fitted to the experimental data with an additional heat loss term which represents the residual heat dissipation $\dot{Q}_{loss,fit}$ = 152 W, see cyan graph. The fit shows high agreement with the experimental data and the fitted heat loss term is a reasonable value compared with $\dot{Q}_{loss,PCB}$ when analyzing the exchange surface area to the PCB and the total to the surrounding. All calculations for Figure 4d are given in Calculation S1. It needs to be stated that temperature differences under adiabatic situations, as in the center of an industrial-scaled stack, may be significantly higher and that the results, especially at high current densities and low water flow rates, need to be considered carefully.

For a deeper understanding of the cell behavior along the channel at different water flow rates, EIS analyses for the extreme conditions at 20 and 2 ml·min^{-1}·cm^{-2} are conducted at a mean current density of 5 A·cm^{-2}, see Figure 5. Figure 5a,b shows the HFR-free impedance spectra along the cell segments for 20 and 2 ml·min^{-1}·cm^{-2}, corresponding to the operating points in Figure 4c. For the high water flow rate, only small temperature or current density gradients exist, and a uniform polarization resistance behavior along the channel is detectable. For the low water flow rate, see Figure 5b, a clear change in the low-frequency impedance along the cell segments can be noticed. It appears that the second inductive feature becomes more pronounced toward the outlet of the cell.

Figure 5c,d shows the Nyquist plots and DRT analysis, for segment 2 and segment 9 of the AtC cell for the two flow rates 2 ml·min^{-1}·cm^{-2} (orange graphs) and 20 ml·min^{-1}·cm^{-2} (blue graphs). To exclude possible boundary effects, segments 1 and 10 are purposely not chosen for this discussion. The results of the ECM fit for segment 2 and segment 9 are given in Figure 5e, f. For high water flow rates at 20 ml·min^{-1}·cm^{-2}, comparable resistances of the four peaks detected by DRT are observed, with only a small decrease of the HFR detected from segment 2 to segment 9. This is expected as no significant gradient in the water-to-gas ratio and temperature is present.

Contrary to this, the HFR decreases more, and the inductive feature changes significantly at 2 ml·min^{-1}·cm^{-2} between segment 2 and segment 9, as already indicated by the temperature profile in Figure 4c. Figure 5f shows that the ASR for both inductive processes ($P_{Pol,3}$ and $P_{Pol,4}$) increases with $P_{Pol,4}$ being more affected at low water flow rates. In Figure 3, we discussed that the inductive feature is increasing with decreasing temperature. Here, we observe an increase in these features with increasing local temperature, as we measured a temperature ∼8 K higher at segment 9 compared to segment 2. Assuming a constant current distribution, the water-to-gas ratio at segment 2 would be ∼50 vol % and at segment 9, <10 vol %. Since the current density is higher at the outlet compared to the inlet, see Figure 4c, the difference in water-to-gas ratio must be even greater. In our previous work on inductive loops,[22] we discussed the inductive feature in relation to membrane and ionomer effects. One possible explanation for the inductive loop could be slow water diffusion coupled with local temperature effects, which both should decrease the protonic cell resistance but are only detectable at low frequencies since the processes have a high time constant and therefore are not included in the HFR measurements.[22] It can be assumed that for all measurements shown here, the ionomer and membrane are humidified well since liquid water is present. Therefore, water diffusion effects might not be significant to the components but may be relevant for internal water transport in the ionomer or membrane. Since we here see a clear increase in the inductive feature with decreasing water amount, we would rather attribute this effect to be a thermal phenomenon. Dynamic fluidic and thermal modeling is suggested to gain a better understanding of the physico-chemical processes behind the inductive low-frequency feature.

Performance Analysis of Different PTLs with a Low-Loading CCM. *Ex Situ Analysis.* In PEM water electrolysis, typically, two different types of titanium-based anode PTLs are commonly used: sintered fiber and sintered particle-based PTLs. Their structural parameters differ significantly in porosity, pore size distribution, and surface properties. Figure 6 shows microstructure analysis results of commercially available PTLs (PTL1 (sintered titanium fiber) and PTL 2 (sintered titanium particle), both with a thickness of 250 μm) and the low-loading CCM produced at the Fraunhofer ISE. Figure 6a shows the 3D μCT scans and Figure 6b the pore size distribution measured by MIP at the University of Gießen for PTL 1 and PTL 2. The extracted parameters are summarized in Table 1. The pore size distributions measured by the two methods are in very good agreement and show significant microstructural differences of the two types of PTLs, which are justified by the different porosity and through-plane tortuosity evaluated from the μCT scans. PTL 2 shows a smaller mean pore size, lower porosity, and higher through-plane tortuosity, which should, in theory, lead to increased gas transport resistance through the porous material. However, the smaller pore sizes may lead to better water transport through the capillary flow. The surface area of PTL 2 is 12% higher than that of PTL 1, see Table 1. The enhanced surface area toward the catalyst layer may significantly improve the catalyst layer and PTL interface as more contact points are available, which increases catalyst utilization and in-plane conductivity. This is especially relevant when measuring with low-loading CCMs.

Figure 6c shows the loading distribution of the catalyst layer of the anode (top) and cathode (bottom) measured by XRF for the Fraunhofer ISE CCMs. The XRF measurement is taken at the center 4 cm × 25 cm² of the catalyst layer; the entire length of the catalyst layer could not be measured due to space limitations of the measurement device. The distribution of the catalyst is very homogeneous over the entire active area with a mean value of (0.20 ± 0.07)mg$_{Ir}$ cm^{-2} at the anode and (0.15 ± 0.03)mg$_{pt}$ cm^{-2} at the cathode. Figure 6d shows the corresponding cross-sectional SEM scan for the CCM. The cathode and anode catalyst layers are zoomed in, revealing a uniform but low catalyst layer thickness of the anode of less than 3 μm. Furthermore, both catalyst layers are very homogeneous. With this analysis, we can neglect the influence of different catalyst layer loadings or significant defects. However, as the structural analysis using SEM cannot be performed across the whole active area, inhomogeneities in the ionomer distribution over the entire active area cannot be entirely excluded.

https://doi.org/10.1021/acsaem.5c00505
ACS Appl. Energy Mater. 2025, 8, 7107−7124

In Situ Analysis of PTL Variation. Figure 7 summarizes the results of the electrochemical characterizations of PTL 1 and PTL 2. All measurements are performed at 60 °C, ambient pressure, and a water flow rate at the anode of 10 ml·min^{-1}·cm^{-2}. To compare the PTLs, we performed measurements with a commercial state-of-the-art CCM and the low-loading CCM produced at Fraunhofer ISE. Figure 7a shows the polarization curves and the HFR-free polarization curves (dashed lines at the bottom). For the commercial CCM based on a 125 μm Nafion membrane (square markers), good performance can be noted by deploying a GDL for the cathode, as described in the Experimental Section. The polarization curves, as well as the HFR-free polarization curves, do not show significant differences between PTL 1 (black) and PTL 2 (red). Regarding the residual overpotentials, see Figure 7b, no significant differences are detectable. The Tafel slope in the legend of Figure 7b shows slightly lower values for PTL 2. This can be explained by the smaller pore size and the higher surface area for PTL 2, which creates more contact points with the catalyst layer and hence increases catalyst layer utilization. The slightly better performance of PTL 2 regarding the residual overpotentials at high current densities can be attributed to the higher in-plane conductivity of the catalyst and the porous transport layer interface. Since the residual overpotentials are decreasing with current density, we assume that mass transport resistances do not have a relevant contribution to the overall polarization. Additionally, by using PTL 2, for which we assume higher gas transport resistance, no significant mass transport related overpotentials are detected. We interpret the decreasing residual overpotential for both cases as indicative of increased ionic in-plane conductivity in the catalyst layer, which should be higher with increasing catalyst layer temperature due to greater heat losses from the reaction.

Using the GDL at the cathode in combination with the low-loading CCM based on a 90 μm thick reinforced PFSA membrane (gray graph with round markers), an enormous increase in overpotentials, especially at low current densities is measured. We attribute this to poor utilization of the catalyst, assuming that contact between the PTL and the thin catalyst layer thickness at the anode (<3 μm, see Figure 6) is difficult to achieve, as already reported in the literature.[64] Even with larger compression of the cell, this issue could not be solved. We believe that when using a soft GDL with a flow field design, as in our case, consisting of 0.9 mm land and 1 mm channel width, the GDL bends into the flow field channel, which decreases the compression or contact between the PTL and the catalyst layer at the anode. This behavior must depend on the contact pressure and should result in large kinetic losses (see the Tafel slope) and high in-plane resistivities (see residual overpotentials). Since most of the electrons are forced to flow along the catalyst layer close to the land areas of the flow field, resulting in a low catalyst utilization due to the poor contact to the PTL. In the case of the commercial CCM, this effect is not observable, which suggests that there are significant differences in catalyst loading, catalyst layer thickness, and catalyst layer in-plane conductivity between the two CCMs employed. Overall, these results underline the importance of well-balanced compression of the PTLs in combination with an optimized interface of the flow field and the PTL (e.g., different channel geometry, stiffer GDL material, or use of a microporous layer (MPL)) to ensure proper catalyst layer utilization with low loadings.

With the use of titanium PTLs at the anode and cathode (see black and red graphs with round markers), the contacting issue is minimized, as significantly higher compression of >4 MPa on the active area can be applied. In the case of using a GDL at the cathode, we compress the cell with only less than 2.5 MPa to minimize damage of the carbon fibers. The polarization curves of the measurement with either PTL 1 or PTL 2 on both sides of the cell show a similar performance, see Figure 7a. The HFR-free polarization curve for current densities <3 A·cm^{-2} also yield equal values. However, for higher current densities, the HFR-free polarization curve differs from each other. The Tafel slope analysis reveals that the cell setup with PTL 2 results in slightly lower values, following the same trend as that in the case of the commercial CCM. The in-house CCM yields larger Tafel slopes for both types of PTLs, which is attributed to the low anode catalyst loading. The residual overpotentials, as depicted in Figure 7b, differ significantly for current densities >3 A·cm^{-2}. We attribute this to a higher in-plane conductivity at the anode in the case of PTL 2 since more contact points of catalyst particles and the PTL are present for this type of PTL. The same trend, albeit less pronounced, can be observed for the commercial CCM.

Figure 7c shows the current density distribution at a mean current density of 3 A·cm^{-2} applied for the low-loading CCM. The current density distribution with the commercial CCM used, and the temperature profiles for both measurements are given in Figure S5. The temperature profiles (see Figure S5) are equal and reveal that PTL 2 results in slightly lower temperatures in all segments with the same tendency as PTL 1 for both types of CCM, which might be explained by better thermal conductivity due to the smaller porosity of PTL 2. The temperature increase along the channel is ∼1 K for all measurements at a current density of 3 A·cm^{-2}. Hence, for the measurements with the commercial CCM, no significant gradients of the current density along the channel can be seen, which can again be attributed to the high water flow rate of 10 ml·min^{-1}·cm^{-2} and, thus, appropriate thermal management.

In the case of the low-loading CCM, no relevant gradient in the current density can be observed for PTL 2. For the measurement with PTL 1, more current flows at the inlet than at the outlet. Therefore, the HFR and MFR along the cell segments for the low-loading CCM in combination with PTL 1 and PTL 2 are analyzed in Figure 7d. In both cases, the HFR is very constant along the channel and only slightly influenced by cell compression issues. For PTL 1, the HFR appears to be slightly higher between segments 6 and 10 compared to segments 1 to 5. However, the HFR itself clearly cannot explain the gradient in current density for PTL 1, as the difference from PTL 2 is marginal. Regarding the MFR of PTL 2, a similar behavior to the HFR is present, which can be interpreted as a constant polarization resistance along the segments. However, for PTL 1, the MFR increases between segments 4 and 6 and remains at this level until segment 9. The current density distribution can therefore be explained by changing the polarization resistances along the channel.

Two characteristic segments for the change in the polarization resistance are segment 3, with the highest, and segment 6 with the lowest performance of all segments for PTL 1. Figure 7e,f shows the impedance of these two segments in Nyquist and DRT presentation for the measurement using PTL 1 (top, black) and PTL 2 (bottom, red). As expected from Figure 7d, the impedance spectra using PTL 2 do not significantly differ between segments 3 and 6; only a slightly

https://doi.org/10.1021/acsaem.5c00505
ACS Appl. Energy Mater. 2025, 8, 7107−7124

increased HFR is detectable. Using PTL 1, a slight increase of the HFR is also observed, but a significant increase in the polarization resistances detected by DRT is noted. Processes below 10 Hz seem to be the most affected. Contrary to the commercial CCMs used, we do not see any low-frequency inductive feature; instead capacitive processes are detectable which are usually associated with mass transport. Since we analyzed the quality of the produced CCM and the PTLs (see the discussion on Figure 6), we would not attribute the difference between segments 3 and 6 using PTL 1 to inhomogeneities in the materials used. Given that the HFR is also slightly affected, contact or compression issues might explain this phenomenon.

To gain a deeper understanding of the effect of different clamping forces for the setup with the low-loading CCM, additional measurements are performed with the Fraunhofer ISE reference cell (active area of 4 cm^2), which was also used in Figure 1. The same cell materials as those used for the AtC cell are deployed (low-loading CCM and either PTL 1 or PTL 2 at the anode and cathode), but the compression force is varied between 0.5 $kN \cdot cm^{-2}$ and 1.125 $kN \cdot cm^{-2}$, with the latter force being equal to the compression in the AtC cell, as determined by pressure paper analysis. Figure 8a shows the impedance spectra for the reference point at 3 $A \cdot cm^{-2}$, 60 °C, ambient pressure, and a water flow rate of 100 $ml \cdot min^{-1}$ only at the anode for PTL 1 (top) and PTL 2 (bottom). The setup with PTL 2 was measured at another, but similar, test bench (the same as that used for the measurement in Figure 1) and with a water flow rate of 150 $ml \cdot min^{-1}$; however, both aspects should not significantly influence our findings regarding the clamping force variation.

With less compression force, the HFR is only slightly affected, while the polarization resistance is significantly impacted; see the analysis of the HFR and MFR in Figure 8b for PTL 1. This perfectly aligns with the phenomenon detected in the AtC cell and allows the conclusion that an unintentionally insufficient compression was given during the AtC measurement with PTL 1. Interestingly, a large impact on the MFR cannot be seen with PTL 2. Compared to the setup with PTL 1, the HFR and MFR only slightly decrease between 2 $kN \cdot cm^{-2}$ and 2.5 $kN \cdot cm^{-2}$ and linearly increase for clamping forces >2.5 $kN \cdot cm^{-2}$. This leads to the assumption that for both AtC cell setups measured, comparable but insufficient compressions were realized, which only have a clear impact on the performance using the setup with PTL 1.

We believe that polarization resistances, including charge transfer, ionic and electronic in-plane resistivity, and mass transport-related phenomena, become more relevant when using low-loading CCMs with thin catalyst layers and comparatively coarse PTLs. This can be explained by the reduction of active area due to inappropriate contact between the catalyst layer and PTL, which cannot be compensated for due to the low catalyst loading, affecting charge transfer and in-plane catalyst layer resistance. Since low-frequency capacitive processes are even more affected, we believe that gas transport between the catalyst layer and PTL is inhibited, resulting in higher mass transport resistance, which might also cause local drying of the ionomer. PTL 2 shows a significantly smoother surface; see the mean pore size and surface area in Table 1. Therefore, these effects seem to be minimized to a certain extent. A better-aligned catalyst layer-PTL interface (e.g., by using an MPL) seems necessary to circumvent these phenomena.

CONCLUSION

In this work, we present a comprehensive voltage breakdown and impedance analysis using DRT with subsequent ECM fitting for a segmented along the channel PEM water electrolysis cell. We varied cell configurations and operational parameters, considering industrially relevant applications. Up to a current density of 7 $A \cdot cm^{-2}$, it is shown that even at relatively low water flow rates of 2 $ml \cdot min^{-1} \cdot cm^{-2}$, corresponding to stoichiometries of 54, no undersupply of water and, therefore, no mass transport limitations occur.

Using the Fraunhofer ISE reference cell with an active area of 4 cm^2, it is shown that for high current densities up to 25 $A \cdot cm^{-2}$, linear polarization curve behavior is still feasible; hence, no mass transport limitations are observable if a sufficient water supply is ensured.

When operating the AtC cell at high current densities >3 $A \cdot cm^{-2}$ in combination with low water flow rates, significant temperature gradients of over 8 K can be detected along the channel, resulting in a substantial impact on the HFR and the impedance toward the outlet of the cell. The increase in temperature results in a performance increase despite lower water stoichiometries, which may increase degradation rates. Theoretical calculations indicate that the temperature gradient would be significantly higher under adiabatic conditions, which may be critical for large-scale industrial stack designs.

The influence of PTLs with different structural parameters combined with a commercial state-of-the-art CCM and a low-loading ("next-generation") CCM produced at Fraunhofer ISE was analyzed. We have demonstrated that on the one hand, PTLs with smaller pore sizes improve catalyst utilization, leading to lower kinetic and residual overpotentials for low-loading CCMs. On the other hand, we did not find significant differences of the structural PTL parameters regarding mass transport-related polarization resistances and conclude that this will play only a minor role for industrial-relevant operation.

Inappropriate cell compression using low-loading CCMs in combination with coarse PTLs surprisingly does not lead to significant differences in the Ohmic resistance. Instead, polarization processes, such as charge transfer, catalyst layer resistivity, and other low-frequency processes as mass transport, are affected, which is proven by clamping pressure variations using the 4 cm^2 cell.

In summary, today's cell components, such as CCM and PTLs, distribute water and gas under industrial-relevant operation points properly, which leads to negligible mass transport-related overpotentials along the channels. This implies a low in-plane flow resistance due to the straight parallel channel flow field design used. Even at high current densities, mass transport issues do not limit the performance. Instead, the limiting factor for high current density operation is the Ohmic cell resistance, which significantly depends on membrane thickness and may result in low cell efficiencies and uneconomic operation. The influence on polarization resistance due to insufficient cell compression seems relevant only when low-loading CCMs are used with thin catalyst layers.

ASSOCIATED CONTENT

Supporting Information

The Supporting Information is available free of charge at https://pubs.acs.org/doi/10.1021/acsaem.5c00505.

Variation of the Tikhonov regularization parameter for DRT analysis; temperature profiles during differential

https://doi.org/10.1021/acsaem.5c00505
ACS Appl. Energy Mater. 2025, 8, 7107−7124

pressure variation; temperature profiles during cell temperature variation; current density and temperature profiles during water flow rate variation; calculation of theoretical heat loss of the along the channel cell; current density and temperature distribution with different PTLs and CCMs (PDF)

AUTHOR INFORMATION

Corresponding Author

Niklas Hensle − *Fraunhofer Institute for Solar Energy System ISE, Freiburg 79110, Germany; Institute for Applied Materials (IAM-ET), Karlsruhe Institute of Technology (KIT), Karlsruhe 76131, Germany;* orcid.org/0009-0001-8308-817X; Email: niklas.hensle@ise.fraunhofer.de

Authors

Jerónimo Horstmann de la Viña − *Fraunhofer Institute for Solar Energy System ISE, Freiburg 79110, Germany*

Nico Winterholler − *Fraunhofer Institute for Solar Energy System ISE, Freiburg 79110, Germany*

Justin Hoffmann − *Fraunhofer Institute for Solar Energy System ISE, Freiburg 79110, Germany*

Stephan Armbruster − *Fraunhofer Institute for Solar Energy System ISE, Freiburg 79110, Germany*

Adrian Lindner − *Institute for Applied Materials (IAM-ET), Karlsruhe Institute of Technology (KIT), Karlsruhe 76131, Germany*

André Weber − *Institute for Applied Materials (IAM-ET), Karlsruhe Institute of Technology (KIT), Karlsruhe 76131, Germany*

Tom Smolinka − *Fraunhofer Institute for Solar Energy System ISE, Freiburg 79110, Germany*

Complete contact information is available at: https://pubs.acs.org/10.1021/acsaem.5c00505

Notes

The authors declare no competing financial interest.

ACKNOWLEDGMENTS

The authors gratefully acknowledge funding from the Federal Ministry of Education and Research, Germany (03HY103F, 03HY103C) and the Ministry of the Environment, Climate Protection and the Energy Sector Baden-Württemberg, Germany (UM BW L7524103). We thank Umesh Anirudh Andaluri for his assistance in carrying out the high current density measurements at Fraunhofer ISE.

REFERENCES

(1) Mohammadi, A.; Mehrpooya, M. A comprehensive review on coupling different types of electrolyzer to renewable energy sources. *Energy* **2018**, *158*, 632−655.

(2) Martinez Lopez, V. A.; Ziar, H.; Haverkort, J. W.; Zeman, M.; Isabella, O. Dynamic operation of water electrolyzers: A review for applications in photovoltaic systems integration. *Renew. Sustain. Energy Rev.* **2023**, *182*, 113407.

(3) Lettenmeier, P.; Wang, R.; Abouatallah, R.; Burggraf, F.; Gago, A. S.; Friedrich, K. A. Proton Exchange Membrane Electrolyzer Systems Operating Dynamically at High Current Densities. *ECS Trans.* **2016**, *72* (23), 11−21.

(4) Lee, H.; Lee, B.; Byun, M.; Lim, H. Economic and environmental analysis for PEM water electrolysis based on replacement moment and renewable electricity resources. *Energy Convers. Manage.* **2020**, *224*, 113477.

(5) Arunachalam, M.; Han, D. S. Efficient solar-powered PEM electrolysis for sustainable hydrogen production: An integrated approach. *Emergent Mater.* **2024**, *7* (4), 1401−1415.

(6) Lettenmeier, P.; Wang, R.; Abouatallah, R.; Helmly, S.; Morawietz, T.; Hiesgen, R.; Kolb, S.; Burggraf, F.; Kallo, J.; Gago, A. S.; Friedrich, K. A. Durable Membrane Electrode Assemblies for Proton Exchange Membrane Electrolyzer Systems Operating at High Current Densities. *Electrochim. Acta* **2016**, *210*, 502−511.

(7) Lewinski, K. A.; van der Vliet, D.; Luopa, S. M. NSTF Advances for PEM Electrolysis - the Effect of Alloying on Activity of NSTF Electrolyzer Catalysts and Performance of NSTF Based PEM Electrolyzers. *ECS Trans.* **2015**, *69* (17), 893−917.

(8) Martin, A.; Trinke, P.; Bensmann, B.; Hanke-Rauschenbach, R. Hydrogen Crossover in PEM Water Electrolysis at Current Densities up to 10 A cm −2. *J. Electrochem. Soc.* **2022**, *169* (9), 94507.

(9) Olesen, A. C.; Frensch, S. H.; Kær, S. K. Towards uniformly distributed heat, mass and charge: A flow field design study for high pressure and high current density operation of PEM electrolysis cells. *Electrochim. Acta* **2019**, *293*, 476−495.

(10) Villagra, A.; Millet, P. An analysis of PEM water electrolysis cells operating at elevated current densities. *Int. J. Hydrogen Energy.* **2019**, *44* (20), 9708−9717.

(11) Siegmund, D.; Metz, S.; Peinecke, V.; Warner, T. E.; Cremers, C.; Grevé, A.; Smolinka, T.; Segets, D.; Apfel, U.-P. Crossing the Valley of Death: From Fundamental to Applied Research in Electrolysis. *JACS Au* **2021**, *1* (5), 527−535. Published Online: Apr. 12, 2021.

(12) Tom, S.What Do We Need in PEM Water Electrolysis to Achieve Our 2030 Targets: A Review of Key Challenges*Berlin Electrolyser Conference*Fraunhofer-Institut für Solare Energiesysteme ISE2023

(13) Lee, J. K.; Lee, C.; Fahy, K. F.; Zhao, B.; LaManna, J. M.; Baltic, E.; Jacobson, D. L.; Hussey, D. S.; Bazylak, A. Critical Current Density as a Performance Indicator for Gas-Evolving Electrochemical Devices. *Cell Rep. Phys. Sci.* **2021**, *2* (5), 100440.

(14) Miličić, T.; Altaf, H.; Vorhauer-Huget, N.; Živković, L. A.; Tsotsas, E.; Vidaković-Koch, T. Modeling and Analysis of Mass Transport Losses of Proton Exchange Membrane Water Electrolyzer. *Processes* **2022**, *10* (11), 2417.

(15) Suermann, M.; Takanohashi, K.; Lamibrac, A.; Schmidt, T. J.; Büchi, F. N. Influence of Operating Conditions and Material Properties on the Mass Transport Losses of Polymer Electrolyte Water Electrolysis. *J. Electrochem. Soc.* **2017**, *164* (9), F973−F980.

(16) Peng, X.; Satjaritanun, P.; Taie, Z.; Wiles, L.; Keane, A.; Capuano, C.; Zenyuk, I. V.; Danilovic, N. Insights into Interfacial and Bulk Transport Phenomena Affecting Proton Exchange Membrane Water Electrolyzer Performance at Ultra-Low Iridium Loadings. *Adv. Sci.* **2021**, *8* (21), No. e2102950. Published Online: Sep. 26, 2021.

(17) Babic, U.; Schmidt, T. J.; Gubler, L. Communication—Contribution of Catalyst Layer Proton Transport Resistance to Voltage Loss in Polymer Electrolyte Water Electrolyzers. *J. Electrochem. Soc.* **2018**, *165* (15), J3016−J3018.

(18) Padgett, E.; Bender, G.; Haug, A.; Lewinski, K.; Sun, F.; Yu, H.; Cullen, D. A.; Steinbach, A. J.; Alia, S. M. Catalyst Layer Resistance and Utilization in PEM Electrolysis. *J. Electrochem. Soc.* **2023**, *170* (8), 84512.

(19) Schuler, T.; Schmidt, T. J.; Büchi, F. N. Polymer Electrolyte Water Electrolysis: Correlating Performance and Porous Transport Layer Structure: Part II. Electrochemical Performance Analysis. *J. Electrochem. Soc.* **2019**, *166* (10), F555−F565.

(20) Weber, C. C.; Schuler, T.; Bruycker, R. D.; Gubler, L.; Büchi, F. N.; Angelis, S. D. On the role of porous transport layer thickness in polymer electrolyte water electrolysis. *J. Power Sources Adv.* **2022**, *15*, 100095.

(21) Hensle, N.; Brinker, D.; Metz, S.; Smolinka, T.; Weber, A. On the role of inductive loops at low frequencies in PEM electrolysis. *Electrochem. Commun.* **2023**, *155*, 107585.

(22) Brinker, D.; Hensle, N.; La Horstmann, D. V.; Franzetti, I.; Bühre; Jerónimo, U. A.; Bühre, L. V.; Andaluri, U. A.; Menke, C.;

Smolinka, T.; Weber, A. Inductive Loops in Impedance Spectra of PEM Water Electrolyzers. *J. Power Sources* **2024**, *622*, 235375.
(23) Schiefer, A.; Heinzmann, M.; Weber, A. Inductive Low-Frequency Processes in PEMFC-Impedance Spectra. *Fuel Cells* **2020**, *20* (20), 499−506.
(24) Gerling, C.; Hanauer, M.; Berner, U.; Friedrich, K. A. Experimental and Numerical Investigation of the Low-Frequency Inductive Features in Differential PEMFCs: Ionomer Humidification and Platinum Oxide Effects. *J. Electrochem. Soc.* **2023**, *170* (1), 14504.
(25) Roy, S. K.; Orazem, M. E.; Tribollet, B. Interpretation of Low-Frequency Inductive Loops in PEM Fuel Cells. *J. Electrochem. Soc.* **2007**, *154* (12), B1378.
(26) Pivac, I.; Barbir, F. Inductive phenomena at low frequencies in impedance spectra of proton exchange membrane fuel cells − A review. *J. Power Sources* **2016**, *326*, 112−119.
(27) Immerz, C.; Bensmann, B.; Trinke, P.; Suermann, M.; Hanke-Rauschenbach, R. Local Current Density and Electrochemical Impedance Measurements within 50 cm Single-Channel PEM Electrolysis Cell. *J. Electrochem. Soc.* **2018**, *165* (16), F1292−F1299.
(28) Hensle, N.; Metz, S.; Weber, A.; Smolinka, T. A Segmented Along the Channel Test Cell for Locally Resolved Analysis at High Current Densities in PEM Water Electrolysis. *J. Electrochem. Soc.* **2024**, *171* (11), 114510.
(29) Immerz, C.; Schweins, M.; Trinke, P.; Bensmann, B.; Paidar, M.; Bystroň, T.; Bouzek, K.; Hanke-Rauschenbach, R. Experimental characterization of inhomogeneity in current density and temperature distribution along a single-channel PEM water electrolysis cell. *Electrochim. Acta* **2018**, *260*, 582−588.
(30) Parra-Restrepo, J.; Bligny, R.; Dillet, J.; Didierjean, S.; Stemmelen, D.; Moyne, C.; Degiovanni, A.; Maranzana, G. Influence of the porous transport layer properties on the mass and charge transfer in a segmented PEM electrolyzer. *Int. J. Hydrogen Energy.* **2020**, *45* (15), 8094−8106.
(31) Dedigama, I.; Angeli, P.; van Dijk, N.; Millichamp, J.; Tsaoulidis, D.; Shearing, P. R.; Brett, D. J. Current density mapping and optical flow visualisation of a polymer electrolyte membrane water electrolyser. *J. Power Sources* **2014**, *265*, 97−103.
(32) Al Shakhshir, S.; Zhou, F.; Kær, S. K. On the Effect of Clamping Pressure and Methods on the Current Distribution of a Proton Exchange Membrane Water Electrolyzer. *ECS Trans.* **2018**, *85* (13), 995−1004.
(33) van der Merwe, J.; Uren, K.; van Schoor, G.; Bessarabov, D. Characterisation tools development for PEM electrolysers. *Int. J. Hydrogen Energy.* **2014**, *39* (26), 14212−14221.
(34) Verdin, B.; Fouda-Onana, F.; Germe, S.; Serre, G.; Jacques, P. A.; Millet, P. Operando current mapping on PEM water electrolysis cells. Influence of mechanical stress. *Int. J. Hydrogen Energy.* **2017**, *42* (41), 25848−25859.
(35) Published Online: Jul. 28, 2022. Reichenauer, G.; Balzer, C.; Meinusch, R.; Smarsly, B. M. Determining Mechanical Moduli of Disordered Materials with Hierarchical Porosity on Different Structural Levels. *Langmuir* **2022**, *38* (31), 9631−9639.
(36) Goh, T. Y.; Basah, S. N.; Yazid, H.; Aziz Safar, M. J.; Ahmad Saad, F. S. Performance analysis of image thresholding: Otsu technique. *Measurement* **2018**, *114*, 298−307.
(37) Boukamp, B. A. A Linear Kronig-Kramers Transform Test for Immittance Data Validation. *J. Electrochem. Soc.* **1995**, *142* (6), 1885−1894.
(38) Feiner, A.-S.; McEvoy, A. J. The Nernst Equation. *J. Chem. Educ.* **1994**, *71* (6), 493.
(39) Kim, P. J.; Lee, J. K.; Lee, C.; Fahy, K. F.; Shrestha, P.; Krause, K.; Shafaque, H. W.; Bazylak, A. Tailoring catalyst layer interface with titanium mesh porous transport layers. *Electrochim. Acta* **2021**, *373*, 137879.
(40) USDE. PEM Water Electrolysis*Hydrogen Production*Millet, P.John Wiley & Sons, Ltd2015
(41) LeRoy, R. L.; Bowen, C. T.; LeRoy, D. J. The Thermodynamics of Aqueous Water Electrolysis. *J. Electrochem. Soc.* **1980**, *127* (9), 1954−1962.
(42) Kurzweil, P.; Dietlmeier, O. *Elektrochemische Speicher: Superkondensatoren, Batterien, Elektrolyse-Wasserstoff, Rechtliche Rahmenbedingungen*; Springer Vieweg, 2018.
(43) Leonide, A.; Sonn, V.; Weber, A.; Ivers-Tiffée, E. Evaluation and Modeling of the Cell Resistance in Anode-Supported Solid Oxide Fuel Cells. *J. Electrochem. Soc.* **2008**, *155* (1), B36.
(44) Schönleber, M.; Klotz, D.; Ivers-Tiffée, E. A Method for Improving the Robustness of linear Kramers-Kronig Validity Tests. *Electrochim. Acta* **2014**, *131*, 20−27.
(45) Zhang, Q.; Wang, D.; Schaltz, E.; Stroe, D.-I.; Gismero, A.; Yang, B. Degradation mechanism analysis and State-of-Health estimation for lithium-ion batteries based on distribution of relaxation times. *J. Energy Storage.* **2022**, *55*, 105386.
(46) Dierickx, S.; Weber, A.; Ivers-Tiffée, E. How the distribution of relaxation times enhances complex equivalent circuit models for fuel cells. *Electrochim. Acta* **2020**, *355*, 136764.
(47) Weiß, A.; Schindler, S.; Galbiati, S.; Danzer, M. A.; Zeis, R. Distribution of Relaxation Times Analysis of High-Temperature PEM Fuel Cell Impedance Spectra. *Electrochim. Acta* **2017**, *230*, 391−398.
(48) Osinkin, D. A. Detailed analysis of electrochemical behavior of high−performance solid oxide fuel cell using DRT technique. *J. Power Sources* **2022**, *527*, 231120.
(49) Chan, A.-L.; Yu, H.; Reeves, K. S.; Alia, S. M. Identifying electrochemical processes by distribution of relaxation times in proton exchange membrane electrolyzers. *J. Power Sources* **2025**, *628*, 235850.
(50) Li, Y.; Jiang, Y.; Dang, J.; Deng, X.; Liu, B.; Ma, J.; Yang, F.; Ouyang, M.; Shen, X. Application of distribution of relaxation times method in polymer electrolyte membrane water electrolyzer. *Chem. Eng. J.* **2023**, *451*, 138327.
(51) Sánchez Batalla, B.; Bachmann, J.; Weidlich, C. Investigation of the degradation of proton exchange membrane water electrolysis cells using electrochemical impedance spectroscopy with distribution of relaxation times analysis. *Electrochim. Acta* **2024**, *473*, 143492.
(52) Maier, M.; Smith, K.; Dodwell, J.; Hinds, G.; Shearing, P. R.; Brett, D. Mass transport in PEM water electrolysers: A review. *Int. J. Hydrogen Energy.* **2022**, *47* (1), 30−56.
(53) Ferriday, T.; Middleton, P. H. Experimental analysis of materials in proton exchange membrane electrolysis cells. *Int. J. Hydrogen Energy.* **2019**, *44* (51), 27656−27663.
(54) Tikhonov, A. N.; Goncharsky, A. V.; Stepanov, V. V.; Yagola, A. G. Numerical methods for the approximate solution of ill-posed problems on compact sets. In Numerical Methods for the Solution of Ill-Posed Problems. Tichonov, A. N.; Gončarskij, A.; Stepanov, V. V.; Jagola, A. G., Eds.; Springer, 1995; Vol. *328*, pp. 65−79. .
(55) Weese, J. A reliable and fast method for the solution of Fredhol integral equations of the first kind based on Tikhonov regularization. *Comput. Phys. Commun.* **1992**, *69* (1), 99−111.
(56) Klotz, D. Negative capacitance or inductive loop? − A general assessment of a common low frequency impedance feature. *Electrochem. Commun.* **2019**, *98*, 58−62.
(57) Rozain, C.; Millet, P. Electrochemical characterization of Polymer Electrolyte Membrane Water Electrolysis Cells. *Electrochim. Acta* **2014**, *131*, 160−167.
(58) Majasan, J. O.; Iacoviello, F.; Cho, J. I.; Maier, M.; Lu, X.; Neville, T. P.; Dedigama, I.; Shearing, P. R.; Brett, D. J. Correlative study of microstructure and performance for porous transport layers in polymer electrolyte membrane water electrolysers by X-ray computed tomography and electrochemical characterization. *Int. J. Hydrogen Energy.* **2019**, *44* (36), 19519−19532.
(59) Garcia-Navarro, J. C.; Schulze, M.; Friedrich, K. A. Measuring and modeling mass transport losses in proton exchange membrane water electrolyzers using electrochemical impedance spectroscopy. *J. Power Sources* **2019**, *431*, 189−204.
(60) Dedigama, I.; Angeli, P.; Ayers, K.; Robinson, J. B.; Shearing, P. R.; Tsaoulidis, D.; Brett, D. In situ diagnostic techniques for characterisation of polymer electrolyte membrane water electrolysers − Flow visualisation and electrochemical impedance spectroscopy. *Int. J. Hydrogen Energy.* **2014**, *39* (9), 4468−4482.

https://doi.org/10.1021/acsaem.5c00505
ACS Appl. Energy Mater. 2025, 8, 7107−7124

(61) Schiller, C. A.; Goehr, H. Faraday-Impedanz als Verknüpfung von Impedanzelementen. *J. Phys. Chem.* **1986**, *148* (1), 105−124.
(62) Wagner, N.; Gülzow, E. Change of electrochemical impedance spectra (EIS) with time during CO-poisoning of the Pt-anode in a membrane fuel cell. *J. Power Sources* **2004**, *127* (1−2), 341−347.
(63) Lickert, T.; Fischer, S.; Young, J. L.; Klose, S.; Franzetti, I.; Hahn, D.; Kang, Z.; Shviro, M.; Scheepers, F.; Carmo, M.; Smolinka, T.; Bender, G.; Metz, S. Advances in benchmarking and round robin testing for PEM water electrolysis: Reference protocol and hardware. *Appl. Energy.* **2023**, *352*, 121898.
(64) Schuler, T.; Weber, C. C.; Wrubel, J. A.; Gubler, L.; Pivovar, B.; Büchi, F. N.; Bender, G. Ultrathin Microporous Transport Layers: Implications for Low Catalyst Loadings, Thin Membranes, and High Current Density Operation for Proton Exchange Membrane Electrolysis. *Adv. Energy Mater.* **2024**, *14* (7), 2302786.

https://doi.org/10.1021/acsaem.5c00505
ACS Appl. Energy Mater. 2025, 8, 7107−7124